Publication Year	2021
Acceptance in OA	2025-03-14T17:42:50Z
Title	A Preliminary Study of Magnetosphere-Ionosphere-Thermosphere Coupling at Jupiter: Juno Multi-Instrument Measurements and Modeling Tools
Authors	Wang, Yuxian, Blanc, Michel, Louis, Corentin, Wang, Chi, André, Nicolas, ADRIANI, Alberto, Allegrini, Frederic, Blelly, Pierre-Louis, Bolton, Scott, Bonfond, Bertrand, Clark, George, Dinelli, Bianca Maria, Gérard, Jean-Claude, Gladstone, Randy, Grodent, Denis, Kotsiaros, Stavros, Kurth, William, Lamy, Laurent, Louarn, Philippe, Marchaudon, Aurélie, Mauk, Barry, MURA, Alessandro, Tao, Chihiro
Publisher's version (DOI)	10.1029/2021JA029469
Handle	http://hdl.handle.net/20.500.12386/36829
Journal	JOURNAL OF GEOPHYSICAL RESEARCH. SPACE PHYSICS
Volume	126

Check for updates

JGR Space Physics

RESEARCH ARTICLE
10.1029/2021JA029469

Key Points:

- We propose a method combining Juno data and modeling to evaluate key parameters of Magnetosphere-Ionosphere-Thermosphere coupling at Jupiter
- We apply this method to eight of the first nine Juno orbits along its trajectories during the main auroral oval crossings
- We derive with this approach a picture of the Magnetosphere-Ionosphere coupling current systems, electric fields and magnitudes of energy transfer rates

Supporting Information:

Supporting Information may be found in the online version of this article.

Correspondence to:

M. Blanc,
michel.blanc@irap.omp.eu

Citation:

Wang, Y., Blanc, M., Louis, C., Wang, C., André, N., Adriani, A., et al. (2021). A preliminary study of Magnetosphere-Ionosphere-Thermosphere coupling at Jupiter: Juno multi-instrument measurements and modeling tools. *Journal of Geophysical Research: Space Physics*, *126*, e2021JA029469. https://doi.org/10.1029/2021JA029469

Received 23 APR 2021
Accepted 2 AUG 2021

© 2021 The Authors.
This is an open access article under the terms of the Creative Commons Attribution-NonCommercial License, which permits use, distribution and reproduction in any medium, provided the original work is properly cited and is not used for commercial purposes.

A Preliminary Study of Magnetosphere-Ionosphere-Thermosphere Coupling at Jupiter: Juno Multi-Instrument Measurements and Modeling Tools

Yuxian Wang[1,2,3], Michel Blanc[3], Corentin Louis[3], Chi Wang[1,2], Nicolas André[3], Alberto Adriani[4], Frederic Allegrini[5,6], Pierre-Louis Blelly[3], Scott Bolton[5], Bertrand Bonfond[7], George Clark[8], Bianca Maria Dinelli[9], Jean-Claude Gérard[7], Randy Gladstone[5], Denis Grodent[7], Stavros Kotsiaros[10], William Kurth[11], Laurent Lamy[12,13], Philippe Louarn[3], Aurélie Marchaudon[3], Barry Mauk[8], Alessandro Mura[4], and Chihiro Tao[14]

[1]State Key Laboratory of Space Weather, National Space Science Center, Chinese Academy of Sciences, Beijing, China, [2]College of Earth and Planetary Sciences, University of Chinese Academy of Sciences, Beijing, China, [3]Institut de Recherche en Astrophysique et Planétologie, Toulouse, France, [4]INAF-Istituto di Astrofisica e Planetologia Spaziali, Rome, Italy, [5]Southwest Research Institute, San Antonio, TX, USA, [6]Department of Physics and Astronomy, University of Texas at San Antonio, San Antonio, TX, USA, [7]Laboratoire de Physique Atmosphérique et Planétaire, STAR Institute, Université de Liège, Liège, Belgium, [8]The Johns Hopkins University Applied Physics Laboratory, Laurel, MD, USA, [9]ISAC-CNR, Bologna, Italy, [10]DTU Space, Technical University of Denmark, Kgs. Lyngby, Denmark, [11]Department of Physics and Astronomy, University of Iowa, Iowa City, IA, USA, [12]Laboratoire d'études spatiales et d'instrumentation en astrophysique, Meudon, France, [13]Laboratoire d'Astrophysique de Marseille, Marseille, France, [14]National Institute of Information and Communications Technology (NICT), Koganei, Japan

Abstract The dynamics of the Jovian magnetosphere are controlled by the interplay of the planet's fast rotation, its main iogenic plasma source and its interaction with the solar wind. Magnetosphere-Ionosphere-Thermosphere (MIT) coupling processes controlling this interplay are significantly different from their Earth and Saturn counterparts. At the ionospheric level, they can be characterized by a set of key parameters: ionospheric conductances, electric currents and fields, exchanges of particles along field lines, Joule heating and particle energy deposition. From these parameters, one can determine (a) how magnetospheric currents close into the ionosphere, and (b) the net deposition/extraction of energy into/out of the upper atmosphere associated to MIT coupling. We present a new method combining Juno multi-instrument data (MAG, JADE, JEDI, UVS, JIRAM and Waves) and modeling tools to estimate these key parameters along Juno's trajectories. We first apply this method to two southern hemisphere main auroral oval crossings to illustrate how the coupling parameters are derived. We then present a preliminary statistical analysis of the morphology and amplitudes of these key parameters for eight among the first nine southern perijoves. We aim to extend our method to more Juno orbits to progressively build a comprehensive view of Jovian MIT coupling at the level of the main auroral oval.

Plain Language Summary Jupiter's magnetosphere is dominated by the presence of a giant magnetized disk of plasma which extends from the orbit of the innermost Galilean moon Io to 50 Jovian radii and more. Plasma motion in this disk is driven mainly by the rotation of the planet and partly by its coupling to the solar wind. The upper atmosphere of the pole and the magnetized disk of plasma are coupled by a system of electric currents (from which the polar aurora is generated). As NASA's Juno spacecraft flies above the northern and southern polar regions every orbit, its different instruments measure magnetic fields, charged particles and auroral emissions. In this article we use data from this suite of instruments taken during the first nine orbits, together with adequate models, to calculate the resistivity of the auroral upper atmosphere and the characteristics of the electric currents closing through it. We also estimate the departure of plasma motions from planetary rotation and the amount of power these currents transfer between the upper atmosphere and magnetized disk.

21699402, 2021, 9, Downloaded from https://agupubs.onlinelibrary.wiley.com/doi/10.1029/2021JA029469 by Cochraneltalia, Wiley Online Library on [26/02/2025]. See the Terms and Conditions (https://onlinelibrary.wiley.com/terms-and-conditions) on Wiley Online Library for rules of use; OA articles are governed by the applicable Creative Commons License

1. Introduction

1.1. The Jovian Magnetosphere, Auroras and Their Coupling Before Juno

The dominant plasma source in the Jovian magnetosphere is Io, which is believed to inject about one ton per second of fresh iogenic ions through volcanism, creating a plasma torus along its orbit (Broadfoot et al., 1979). The dynamics and general circulation of this cold plasma in the Jovian magnetosphere are mainly controlled by the fast rotation of the planet (in ∼10 h), while solar wind-magnetosphere coupling plays a secondary role (Delamere & Bagenal, 2010; Vasyliunas, 1983). As the Iogenic plasma is picked up and accelerated into corotation with the planet, it is also transported outward by a centrifugal interchange instability and other radial transport processes, forming a magnetodisk confined near the centrifugal equator (Bagenal & Delamere, 2011; Bolton et al., 2015; Kivelson & Southwood, 2005; Kivelson et al., 2004). Prior to the Juno mission, observations of magnetospheric dynamics such as plasma flow patterns (e.g., Krupp et al., 2001) and reconnection signatures (e.g., Vogt et al., 2010) were mainly provided by the Galileo spacecraft and limited to the vicinity of the centrifugal equator.

During the pre-Juno period, observations of Jovian auroral emissions were first obtained in the radio wavelengths (Bigg, 1964; Burke & Franklin, 1955; Gurnette et al., 1983; Kurth et al., 1997; Stone et al., 1992; and see e.g., Kurth, 1992; Zarka, 1998, 2004 for exhaustive reviews). Prominent emissions were then observed at other wavelengths. For example, X-ray emissions were observed using the Einstein observatory (Metzger et al., 1983), Röntgen satellite (ROSAT, Waite et al., 1994) and later Chandra (Gladstone et al., 1998) and X-ray Multi-Mirror Mission (XMM-Newton, see Wibisono et al., 2020 and references therein). Emissions at ultraviolet (UV) and infrared (IR) wavelengths were mainly obtained from the Hubble Space Telescope (HST, Clarke et al., 1998; Gérard et al., 2014) and ground-based telescopes (Drossart et al., 1989; Stallard et al., 2003, 2018), respectively. HST UV images showed that the Jovian aurora consists of three main components with approximately equal contributions to the total power (Grodent et al., 2018), that is, with increasing latitudes, (a) a mix of diffuse, patchy and sometimes arc-like auroral emissions, which includes the satellite footprints, (b) a relatively stable auroral main oval, and (c) variable emissions poleward of the main oval, though the real auroral morphologies are further complicated by some finer structures (e.g., Grodent, 2015 and references therein).

Based on these separate data sets, a global 3-dimensional picture of the dynamics of the Jovian magnetosphere has emerged before the Juno mission, which connected these different elements into a consistent picture, as illustrated in Figure 1 (adapted from Bagenal et al., 2017). The equatorial plane cross-section (panel a) shows the dominance of a broad corotation-dominated plasma flow within radial distances of about 50 R_J (Jovian radius, $1R_J$ = 71,492 km), with increasing departures from corotation beyond approximately 20 R_J. Beyond ∼50 R_J (outer magnetosphere and magnetotail), the interaction with the solar wind becomes increasingly important or dominant. The noon-midnight meridian plane cross-section (panel b) shows that the plasma in the equatorial plane is magnetically linked to the different regions of auroral emissions (blue lines in the figure draw the magnetic field).

1.2. Introduction to MIT Coupling

The dynamics of the Jovian magnetosphere (illustrated in Figure 2) are controlled by Magnetosphere-Ionosphere-Thermosphere (MIT) coupling processes, involving the transmission of electromagnetic fields and waves, flow of electric currents and transport of particles between the three regions described in the figure. Specifically, these three regions are the equatorial magnetosphere region dominated by the dynamics of the magnetodisk (we will call it Region I), the high-latitude polar and auroral magnetosphere threaded by polar and auroral magnetic field lines (Region II), and the ionosphere/thermosphere (region III). These regions are dynamically coupled by processes operating mainly along the magnetic field (left-hand column of Figure 2). In this work we use the JRM09 magnetic field model (Connerney et al., 2018) and the CAN81 current sheet model (Connerney et al., 1981) to connect the magnetic field in the magnetosphere ($\vec{B}_{\mathrm{mag}}$) to its ionospheric counterpart ($\vec{B}_{\mathrm{iono}}$).

In the quasi-static approximation of electrodynamics, the electric field ($\vec{E}$) and its electrostatic (ES) potential (Φ) are mapped along magnetic field lines between the magnetosphere and ionosphere (second

21699402, 2021, 9, Downloaded from https://agupubs.onlinelibrary.wiley.com/doi/10.1029/2021JA029469 by CochraneItalia, Wiley Online Library on [26/02/2025]. See the Terms and Conditions (https://onlinelibrary.wiley.com/terms-and-conditions) on Wiley Online Library for rules of use; OA articles are governed by the applicable Creative Commons License

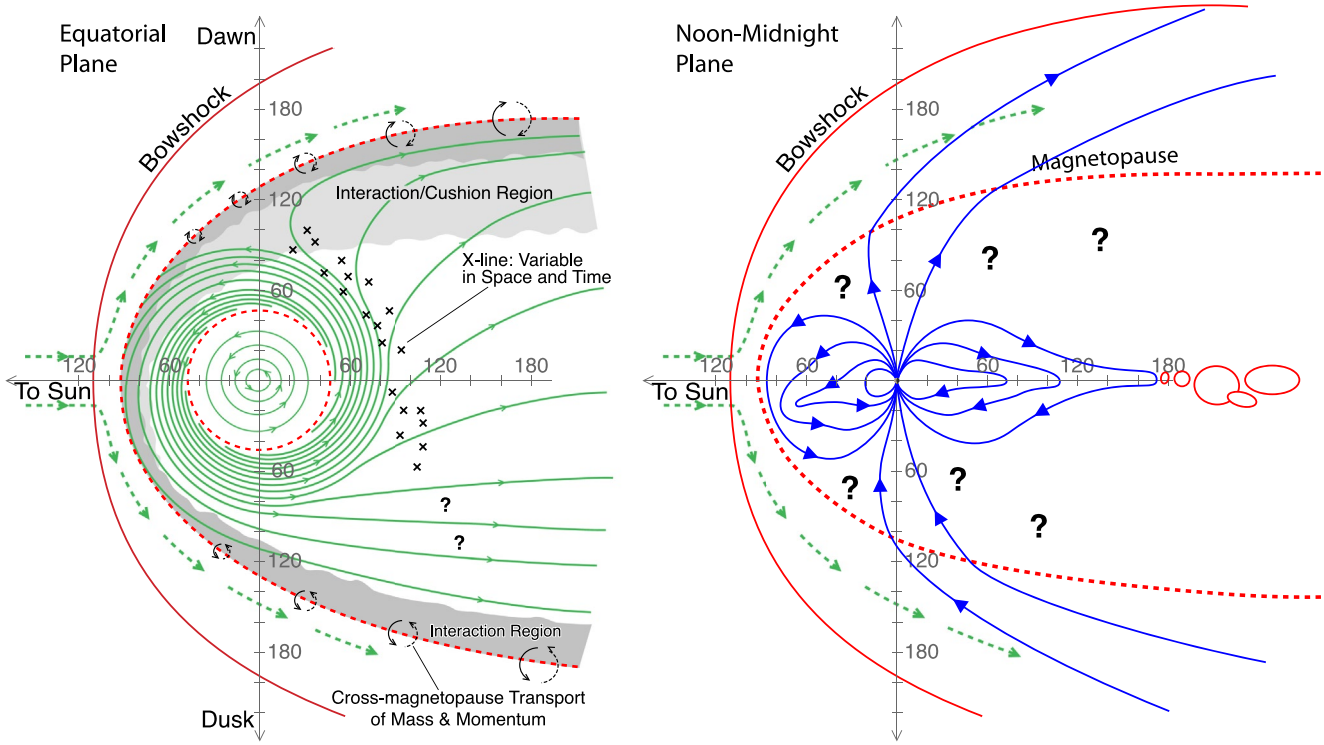

Figure 1. A schematic representation of the Jovian magnetospheric structure and dynamics obtained prior to Juno in the equatorial plane (a) and in the noon-midnight plane (b). Blue lines show the magnetic field, green lines indicate flows and red lines show boundaries between plasma regimes (magnetopause and bow shock). The red circles in panel (b) represent the plasmoids related to the tail reconnection in the Vasyliunas cycle. Adapted from Bagenal et al. (2017).

column from left in Figure 2). This mapping must take into account possible local decoupling by magnetic-field-aligned electric fields ($\vec{E}_{\parallel}$) and the corresponding electrostatic potential drops in the high-latitude polar regions (Mauk et al., 2020). The third column from left in Figure 2 shows how electric currents close: Electric currents $\vec{J}_{\mathrm{mag}}$ flowing in the equatorial magnetosphere are connected with magnetic-field-aligned

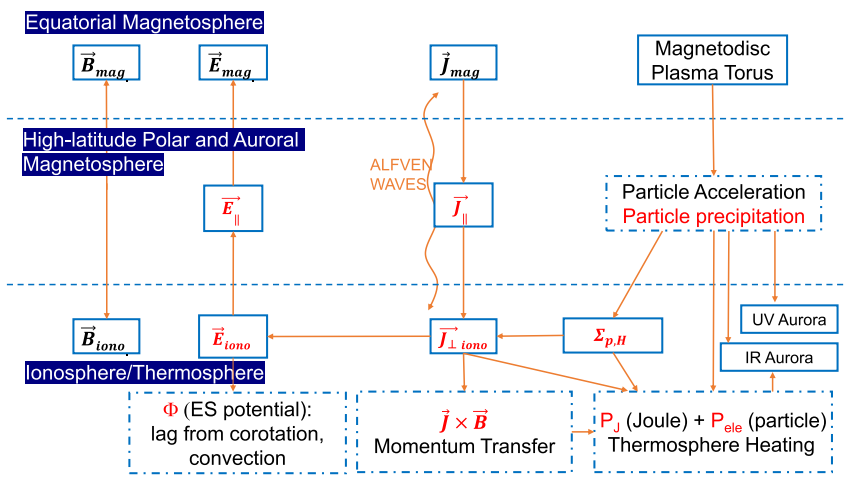

Figure 2. A schematic of the key coupling processes involved in Magnetosphere-Ionosphere-Thermosphere coupling, showing the main physical quantities/objects (solid boxes) and some of the associated processes (dash-dotted boxes) involved in the coupling of the three regions limited by the horizontal dashed lines: equatorial magnetosphere, high-latitude polar and auroral magnetosphere, and ionosphere/thermosphere. From left to right, these three regions are coupled, mainly along magnetic field lines, by means of transmission of electric fields ($\vec{E}$), closure of electric currents ($\vec{J}$) and exchange of particles.

21699402, 2021, 9, Downloaded from https://agupubs.onlinelibrary.wiley.com/doi/10.1029/2021JA029469 by Cochraneltalia, Wiley Online Library on [26/02/2025]. See the Terms and Conditions (https://onlinelibrary.wiley.com/terms-and-conditions) on Wiley Online Library for rules of use; OA articles are governed by the applicable Creative Commons License

currents (FACs) ($\vec{J}_{\parallel}$) which balance their local divergence. These FACs finally close through the two magnetically conjugate ionospheric conductors as ionospheric horizontal currents ($\vec{J}_{\mathrm{iono}}$). Khurana (2001) used magnetic field measurements from Galileo to estimate these FACs and found that the two current systems that close into the ionosphere, that is, the radial currents and the Region 2 currents, were broadly of the same magnitude (~60–100 MA). These current "loops" connecting $\vec{J}_{\mathrm{mag}}$ to $\vec{J}_{\mathrm{iono}}$ control the amount of momentum transfer between the magnetosphere and ionosphere by the effect of the associated Lorentz force ($\vec{J} \times \vec{B}$). Finally, the right-hand column of Figure 2 describes part of the transport of particles between equatorial magnetosphere and ionosphere along field lines: some of the particles in the magnetodisc and plasma torus are scattered into the loss cone, transported to the high-latitude regions and finally precipitate into the upper atmosphere, experiencing acceleration in some regions during this transport (e.g., Mauk et al., 2020). These precipitating particles generate ion-electron pairs via collisions with thermospheric neutrals, thus enhancing Pedersen/Hall conductances of the ionosphere, inducing the UV aurora, and heating the thermosphere via Joule heating (P_J) and particle precipitation (P_{ele}, precipitating electron energy flux). Thermospheric heating in turn affects the excitation of rovibrational levels of H_3^+ ions and thus the IR emissions (Drossart et al., 1989; Stallard et al., 2003, 2018). In summary, as shown in the successive columns from left to right of Figure 2, these three regions are coupled by means of transmission of electric fields, closure of electric currents and exchange of particles along the magnetic field lines connecting them.

Several processes may combine to add complexity to this simplified description. First, when the conditions for the validity of the quasi-static approximation of electrodynamics are not fulfilled, the transmission of electric fields and currents may be mediated by Alfvén waves (see Saur et al., 2018). This may happen when the flow evolution time constants are comparable to Alfvén propagation times along field lines between the ionosphere and magnetodisk. Measurement of the magnetic field turbulences by Juno indeed showed that Alfvén waves are a significant contributor to the main auroral emissions at Jupiter (Gershman et al., 2019). Second, electric currents flowing along magnetic field lines, that is, FACs, are carried by the motion of charged particles, mostly electrons which offer the highest mobility parallel to the magnetic field. In the complex and turbulent medium which populates polar and auroral magnetic field lines, a host of mechanisms can generate electric fields along these field lines and accelerate particles upward, downward (with respect to Jupiter), or many times in both directions, as observed by Juno (Mauk et al., 2020). These effects, which must be kept in mind in our analysis of Juno data, may generate some degree of decoupling between the magnetodisk and its magnetically conjugate ionospheres, for instance via field-aligned electrostatic potential drops.

MIT coupling will be captured in our study as a set of "key parameters" (shown in Table 1) characterizing the transmission of electric fields, electric currents and particles between the three regions, which provide a fair representation of the drivers and effects of MIT coupling at the ionospheric ends of field lines.

In the simplified case of an axisymmetric Jovian magnetosphere driven solely by planetary rotation enforced via the thermosphere and its ionospheric conductor, MIT coupling can be described in terms of a corotation enforcement current loop connecting the magnetodisk and the ionospheric conductor via FACs (Cowley & Bunce, 2001; Hill, 2001; Nichols & Cowley, 2004; Southwood & Kivelson, 2001). Electric currents flowing radially away within the magnetodisk accelerate the plasma via the Lorentz force ($\vec{j} \times \vec{B}$) to partly maintain corotation, thus compensating for the loss of angular velocity of the plasma produced by its radial outward flow from the Io torus. These radial currents diverge into FACs (Cowley & Bunce, 2001; Hill, 2001) which close through the ionosphere as ionospheric currents. The Lorentz force associated with these currents tends to decelerate the corotational flow of the ionosphere and thermosphere, thus extracting angular momentum out of the Jovian upper atmosphere and transmitting it to the magnetodisk. The intensities of all currents in this simplified corotation-enforcement current loop are modulated by the magnitudes of ionospheric conductances, which are enhanced at high latitudes by polar and auroral electron precipitation. This simplified axisymmetric description of MIT coupling at Jupiter represents a useful reference case.

21699402, 2021, 9, Downloaded from https://agupubs.onlinelibrary.wiley.com/doi/10.1029/2021JA029469 by CochraneItalia, Wiley Online Library on [26/02/2025]. See the Terms and Conditions (https://onlinelibrary.wiley.com/terms-and-conditions) on Wiley Online Library for rules of use; OA articles are governed by the applicable Creative Commons License

Table 1
The Key Parameters of MIT Coupling at the Ionospheric Level to be Evaluated in This Study

MIT coupling parameters	Description
Transmission of electric fields	
$\vec{E}_{\text{iono}}$	Horizontal ionospheric electric field.
Φ	Ionospheric electrostatic potential.
$\overrightarrow{E_{\parallel}}$	Electrostatic field along field lines - not directly accessible.
Closure of electric currents	
$\overrightarrow{J_{\parallel}}$	Field Aligned Current (FACs) at the top of ionosphere.
$\vec{J}_{\perp,\text{iono}}$	Horizontal height-integrated ionospheric current.
$\Sigma_{P,H}$	Pedersen and Hall ionospheric conductances.
Exchange of particles	
Net upward and downward fluxes of electrons and ions along magnetic field lines.	
Energy input into the upper atmosphere	
P_{ele}	Particle precipitation.
P_J	Joule heating.

1.3. Juno as a Probe of MIT Coupling: Instrument Suite and Orbital Characteristics

NASA's Juno mission, launched in August 2011 and injected into a 53-day near-polar Jovian orbit in July 2016, is the first spacecraft to explore the Jovian polar magnetosphere and observe its auroral emissions close-in (Bagenal et al., 2017; Bolton et al., 2017). Thanks to its polar orbit, Juno is closing the observational gap between magnetospheric dynamics and auroral emissions. It provides for the first time the observations needed to derive the key physical quantities characterizing MIT coupling processes in the Jovian ionosphere (shown in Table 1). These new observations also challenged the prominence of the corotation enforcement currents as well as axisymmetric and steady-state processes in the magnetosphere-ionosphere coupling (Bonfond et al., 2020).

Juno's science payload includes a suite of fields-and-particles instruments performing in-situ observations, and two remote sensing instruments for auroral imaging. The electron energy and pitch angle distribution functions used in this study are obtained in situ from the Jovian Auroral Distributions Experiment (JADE, electrons: 0.1–100 keV; ions: 5–50 keV; McComas et al., 2017) and the Juno Energetic particle Detector Instrument (JEDI, electrons: 30–800 keV; ions: 10 keV to >1 MeV; Mauk et al., 2017). The magnetic field data is provided by the Juno magnetic field investigation (MAG; Connerney et al., 2017). Jovian radio and plasma waves are measured by the Waves instrument covering the spectrum from 50 Hz to >40 MHz (Kurth, Imai, et al., 2017).

Remote sensing observations of the aurora are provided by two spectral imagers, one in the UV and one in the IR wavelength ranges. UVS is a long-slit Ultraviolet Spectrograph with wavelengths between 68 and 210 nm (Gladstone et al., 2017). Because auroral UV emissions are a tracer of instantaneous energy inputs of electron precipitations, techniques have been developed to derive their characteristic energy and energy flux from UVS observations (e.g., Gérard et al., 2019). The Jupiter Infrared Auroral Mapper (JIRAM) analyses the 2–5 μm range of atmospheric emissions (Adriani, Filacchione, et al., 2017), within which infra-red emissions by H_3^+ and CH_4 can be observed. H_3^+ emissions can be used to derive the temperature and column density of H_3^+ (e.g., Adriani, Mura, et al., 2017; Dinelli et al., 2017) in the regions where it is excited, and the imaging of auroral emissions (Mura et al., 2017) is useful to identify the context of spectral data. In addition, Moriconi et al. (2017) showed that, outside the regions of strong H_3^+ emission and particularly inside the ovals in some areas of the polar caps, CH_4 and H_3^+ emissions can be disentangled to isolate the

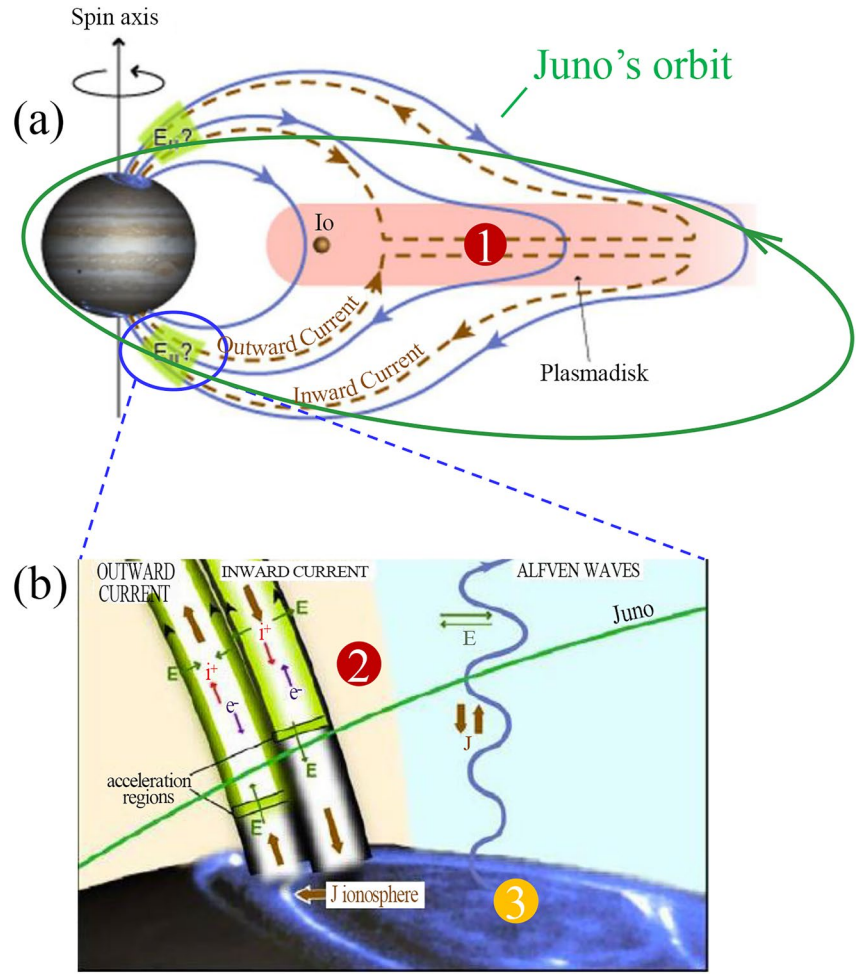

Figure 3. Illustration of Jovian Magnetosphere-Ionosphere-Thermosphere (MIT) coupling processes connecting the equatorial magnetosphere, high-latitude polar and auroral magnetosphere, and ionosphere/thermosphere introduced in Figure 2. (a) Sketch of the meridian cross-section of the Jovian magnetosphere. The blue solid lines indicate magnetic field lines, and the brown dashed curves show the two current loops connecting each hemisphere's ionosphere to the magnetodisk by means of magnetic-field-aligned currents (FACs). The magnetodisk plasma, fed mainly by plasma transported radially outwards from the Io torus, is represented by the red shading (Adapted from Cowley & Bunce, 2001). (b) A close-up view of the Jovian ionosphere showing the main physical processes involved in MIT coupling: upward and downward FACs and particle acceleration processes related to field-aligned electrostatic potential drops and/or to Alfvén waves. The green curves in both panels represent Juno's trajectory. Note here that Juno's orbit is not to scale (Adapted from Bagenal et al., 2017).

emission of CH_4, from which the vibrational temperature of this molecule can be obtained. Under the reasonable assumption of Local Thermodynamic Equilibrium (LTE), this emission provides the kinetic temperature of the neutral gas in the polar caps, a useful input to adjust an atmosphere model.

Figure 3 shows the axisymmetric corotation-enforcement current loop model of MIT coupling (Cowley & Bunce, 2001) described in Section 1.2. This figure illustrates the unique way by which the combination of Juno's polar eccentric orbit and science payload allow one to monitor the three regions of space involved in MIT coupling ([a] equatorial magnetosphere, [b] high-latitude polar and auroral magnetosphere, and [c] ionosphere/thermosphere) and to determine the key parameters of this coupling at ionospheric altitudes listed in Table 1.

Juno was placed on a near-polar orbit with a period of 53 days, a perijove of about 0.05 R_J above Jupiter's one-bar level atmosphere, and an apojove of about 100 R_J, thus crossing the main MIT coupling regions during each orbit. Juno usually crosses the magnetodisk several times because of the effect of Jupiter's tilt of

21699402, 2021, 9, Downloaded from https://agupubs.onlinelibrary.wiley.com/doi/10.1029/2021JA029469 by CochraneItalia, Wiley Online Library on [26/02/2025]. See the Terms and Conditions (https://onlinelibrary.wiley.com/terms-and-conditions) on Wiley Online Library for rules of use; OA articles are governed by the applicable Creative Commons License

21699402, 2021, 9, Downloaded from https://agupubs.onlinelibrary.wiley.com/doi/10.1029/2021JA029469 by Cochraneltalia, Wiley Online Library on [26/02/2025]. See the Terms and Conditions (https://onlinelibrary.wiley.com/terms-and-conditions) on Wiley Online Library for rules of use; OA articles are governed by the applicable Creative Commons License

Table 2
The Different Juno Data Products Used in Our Method

Instrument	Data products
JADE and JEDI	1. Electron differential particle flux (intensities)
	2. Electron pitch angle distribution
MAG	1. Magnetic field vector
	2. Magnetic perturbations
UVS	1. Auroral brightness along the Juno footprint
	2. Color ratio along the Juno footprint
	3. Global map of the orthographic polar projections at an altitude of 400 km above the 1-bar level for the UV intensities and color ratios
	4. 2D Pedersen conductance distribution
JIRAM	1. Orthographic map of the integrated intensities of IR emission
	2. Distribution of H_3^+ column density
	3. Thermospheric effective temperature deduced from H_3^+ emissions.
Waves	1. Frequency-time spectrograms of the electric field spectral density
	2. Frequency-time spectrograms of the magnetic field spectral density
	3. E/cB ratio

magnetic dipole axis with respect to the spin axis, and also flies successively above the northern and southern polar caps and auroral regions at each perijove. In this initial study, we will use only eight of the first nine orbits (without the second orbit when the instruments were off), for which all data have been posted on NASA's Planetary Data System (PDS). The perijoves will be labeled as PJ-nS for the southern hemisphere and PJ-nN for the northern hemisphere, *n* being the orbit number.

1.4. Objectives of This Study and Organization of the Article

In this paper, we present a new systematic method to derive and evaluate the key MIT coupling parameters (listed in Table 1), using a synergistic approach combining Juno data taken during eight of the first nine perijoves along with appropriate models. We establish a preliminary picture of their morphologies, orders of magnitude and relationships.

The paper is organized as follows. Our general methodology is described in Section 2, and the main results are presented in Section 3. The validity of the method and implications of the results are discussed in Section 4. Section 5 gives a summary and some conclusions. A detailed description of the modeling tools involved in this study is presented in the appendices.

2. Methodology

2.1. Overview of Juno Data Product Inputs

The different Juno data products used in our method are listed in Table 2. While all in-situ data are acquired simultaneously, the imaging data may correspond to slightly different times of up to several minutes. However, the effects of these time lags on the morphology of the aurora should be minor because Jupiter's main oval emissions are known to be relatively stable over timescales of tens of minutes to hours (e.g., Allegrini et al., 2020; Mura et al., 2017).

Electron differential fluxes representative of their average values in the loss cone are obtained from intercalibrated JADE and JEDI data, following Allegrini et al. (2020), in order to cover the full ~100 eV–1 MeV energy range without significant discontinuity over the energy range where the two instruments overlap.

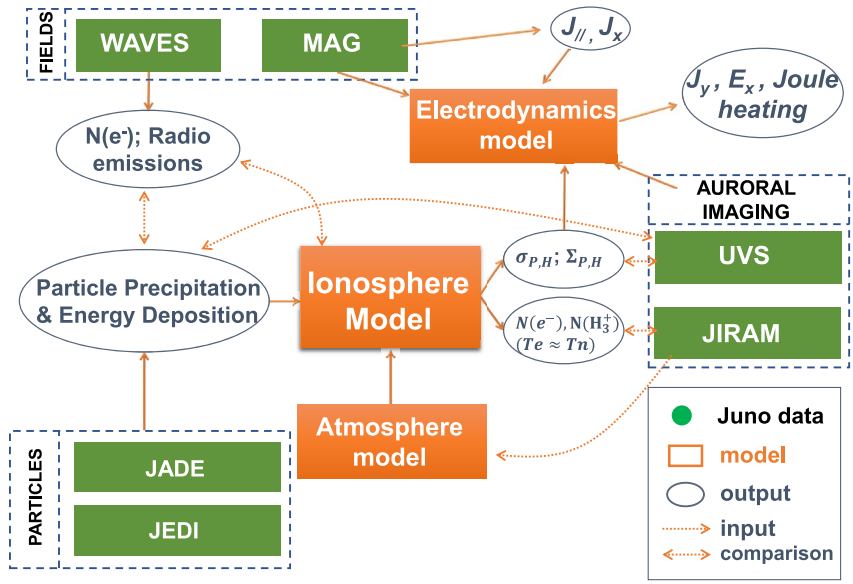

Figure 4. Schematic of the method used to retrieve the key parameters of Magnetosphere-Ionosphere-Thermospherecoupling from Juno data (green boxes) and modeling tools (orange boxes). Using the electron precipitation data obtained from the Juno JADE and JEDI measurements, some of the ionospheric parameters such as conductivities and electron/ion densities can be calculated from the ionosphere model. The electrodynamics model along with the Juno WAVES and MAG data can be used to evaluate the ionospheric currents and Joule heating. The auroral imaging data provide information on the electron precipitations and atmospheric heating, which can be used as a comparison with the results obtained using our method.

2.2. Overview of the Three Models

As shown in Figure 4 (orange boxes), there are three models involved in our method.

The first model is a semi-empirical atmosphere model based on an Earth atmosphere model (Banks & Kockarts, 1973), described in Appendix A-1 in the Supporting Information S1. Its main assumptions are vertical hydrostatic equilibrium, diffusive equilibrium of each species above the homopause, a well-mixed chemically homogeneous atmosphere below the homopause, and the existence of a hydrocarbon layer. Several of the modeled species (atomic H, C_2H_2) are generated locally in the upper atmosphere by the photodissociation of CH_4 and of H_2. The original Earth atmosphere model was initially adapted to Jupiter based on Galileo data by Blelly et al. (2019). In this study, the model is further improved by introducing more neutral species and by an extensive parameterization. As a result, the improved model includes five neutral species (H, H_2, H_e, CH_4, and C_2H_2) and has 17 free parameters that can be adjusted to observational data from Juno and possibly other sources.

The second model is an ionosphere model, described in Appendix A-2 in the Supportinhg Information S1, which is based on the model by Hiraki and Tao (2008) and similar to the model used by Gérard et al. (2020, 2021) to provide estimates of Pedersen conductances from UVS observations. The main differences are that we use the JADE and JEDI electron measurements as inputs for the calculation of the H_3^+ production rate and thus the conductivities. The precipitating energy flux measured by Juno's particle instrument in the polar regions inside the main ovals greatly underestimates the precipitating energy flux required to explain the UV emissions, possibly partly because Juno flew above the acceleration region, and partly because the shapes of electron energy spectra used for the derivation of precipitation fluxes from UVS data may differ from the real ones (see discussion section below). However, the match is generally better for the main emissions (Gérard et al., 2019), which are those we are studying here. In this model the ionization source is limited to electron precipitation, the continuous slow-down approximation is used to calculate the ion-electron pair production function, and we assume that the ionospheric plasma is in local equilibrium, neglecting transport. A simplified ion chemistry is used: The atmosphere model only includes H_2 and CH_4, and we assume that CH_5^+ ions are the final products of ion-neutral chemical reactions at low altitudes.

21699402, 2021, 9, Downloaded from https://agupubs.onlinelibrary.wiley.com/doi/10.1029/2021JA029469 by Cochraneltalia, Wiley Online Library on [26/02/2025]. See the Terms and Conditions (https://onlinelibrary.wiley.com/terms-and-conditions) on Wiley Online Library for rules of use; OA articles are governed by the applicable Creative Commons License

21699402, 2021, 9, Downloaded from https://agupubs.onlinelibrary.wiley.com/doi/10.1029/2021JA029469 by CochraneItalia, Wiley Online Library on [26/02/2025]. See the Terms and Conditions (https://onlinelibrary.wiley.com/terms-and-conditions) on Wiley Online Library for rules of use; OA articles are governed by the applicable Creative Commons License

The third model is the electrodynamics model, described in Appendix A-3 in the Supporting Information S1. This model assumes current continuity between FACs and ionospheric currents, using the ionospheric Ohm's law. Magnetic field perturbations from Kotsiaros et al. (2019) are used to calculate FACs and ionospheric currents orthogonal to the auroral oval under the assumption that variations along the oval are small compared to variations across it, neglecting "slow" variations of electrodynamic parameters at the scale of the planetary radius or larger. Based on this assumption, we can derive the other key parameters of MIT coupling listed in Table 1 from the Ohm's law and current continuity equations, using the conductances calculated by the ionosphere model.

2.3. Description of Our Method to Retrieve the Key Parameters From Juno Data and Models

Our general approach for each specific auroral crossing by Juno is illustrated in Figure 4. Specifically, we use simultaneous in-situ and imaging data from Juno (in green) as inputs to the three basic models (orange boxes) described in Section 2.2, that is, an atmosphere model, an ionosphere model and an electrodynamics model, to retrieve the MIT coupling key parameters.

Let us describe the major steps in the derivation of MIT coupling key parameters. First, our Jovian neutral atmosphere model can be determined using the H_3^+ temperature derived from JIRAM imaging data outside the regions of strong Joule heating when available, under the assumption of thermal equilibrium between ions and neutrals which is reasonable in the lower ionosphere where electric currents flow. However, there was no adequate JIRAM data that could be used for most of the first nine perijoves, and our neutral atmosphere model was simply adjusted to the Grodent et al. (2001) model, leaving the adjustment to JIRAM data for a future study.

We then derive the electron precipitation spectrum on each magnetic field line monitored by Juno by combining the JADE and JEDI electron data sets and using a nominal 2-s time resolution. After that, we inject this spectrum together with our modeled neutral atmosphere into the ionosphere model to calculate the ion production functions, the number densities of electrons and ions and the Pedersen and Hall conductivities as a function of altitude. Height-integrated Pedersen and Hall conductivities are calculated via an integration in altitude of these conductivities throughout the ionosphere. Finally, using magnetic field measurements from MAG and the calculated conductances, all other parameters including FACs, ionospheric electric currents and fields, Joule heating, are derived from the electrodynamics model.

In addition, some of these parameters can be derived from Waves data, which may be used for comparison and validation. For example, Waves data give access to the electron densities n_e at Juno's position (Tetrick et al., 2017) from inspection of the high-frequency cut-off of the auroral hiss emission, which is a function of the electron plasma frequency $\left(f_{\mathrm{pe}}\right)$. Thus, the Waves data can provide a complementary information to JADE measurements, which can also provide electron densities over the polar regions: see Sulaiman et al. (2021) for the method and Elliott et al. (2021). A more detailed description of this method is given in Appendix A-3 in the Supporting Information S1. Waves data also make it possible to monitor directly the radio emission sources when Juno crosses them, and to relate them to electron distribution functions feeding them (Kurth, Hospodarsky, et al., 2017; Louarn et al., 2017, 2018; Louis et al., 2019). It should be noted that in our current preliminary study, the Waves data are not used to obtain the electron density information (but only to determine the presence of auroral radio emission): this is left for the next step in the development of our method.

2.4. Characteristics of the Perijoves Selected for This Study

In this study, multi-instrument Juno data are used to provide a near synchronous observation of the Jovian polar magnetosphere and ionosphere. Since we calculate ionospheric currents based on the assumptions of slow variations along the main oval compared to variations across the oval, the magnetic field and auroral morphologies of the southern polar cap better fulfill this assumption, and for this reason we selected only southern perijoves for this preliminary study. The selected time intervals and some basic parameters for the eight selected southern auroral crossings are listed in Table 3. For all these perijoves electron loss cones can be well resolved by JADE and JEDI measurements, thus allowing the calculation of conductances from particle precipitation observations.

21699402, 2021, 9, Downloaded from https://agupubs.onlinelibrary.wiley.com/doi/10.1029/2021JA029469 by CochraneItalia, Wiley Online Library on [26/02/2025]. See the Terms and Conditions (https://onlinelibrary.wiley.com/terms-and-conditions) on Wiley Online Library for rules of use; OA articles are governed by the applicable Creative Commons License

Table 3
The Selected Time Intervals and Some Basic Parameters Used in This Study

PJ (south)	Date	Time intervals of this study		Maximum loss cone angle (deg)	MLT (hr.)	R (RJ)	M-shell (JRM09 + CAN81)
		Start	End				
1	2016-240	13:24	13:41	35	15.63–16.71	1.52–1.87	08.1–75.1
3	2016-346	17:33	17:41	39	17.00–17.29	1.43–1.61	08.4–61.3
4	2017-033	13:33	13:45	35	18.22–19.31	1.56–1.83	09.0–68.2
5	2017-086	09:36	09:53	28	16.89–17.37	1.76–2.14	10.5–91.0
6	2017-139	06:49	07:02	27	15.26–15.55	1.87–2.15	19.8–75.2
7	2017-192	02:25	02:41	37	13.88–15.30	1.46–1.82	07.8–69.9
8	2017-244	22:21	22:34	36	16.46–16.72	1.50–1.77	06.8–79.3
9	2017-297	18:25	18:44	28	16.15–17.00	1.72–2.17	08. 4–93.2

3. Results

3.1. Preliminary Analysis of the Relationship Between Conductances and Auroral Electron Precipitation

As mentioned in Section 1.2, precipitating particles in auroral regions have two different but simultaneous effects on the current systems driven by this coupling: On the one hand, as current carriers, they contribute to the FACs which close through the ionospheric conductor; on the other hand, they create ion-electron pairs and thus modulate ionospheric ion and electron number densities and the conductances of the ionosphere. In order to better understand the relationship between Pedersen/Hall conductances and precipitating particle energies, we calculated the ionospheric conductances produced by a monoenergetic beam of electrons of varying incident energy, for a constant incident electron energy flux of 100 mW/m^2. Note that 100 mW/m^2 is the typical downward electron energy flux observed within the main auroral regions in this study (see the top panels of Figures 7 and 8). The results, based on the ionospheric model described in Section 2, are shown in Figure 5. To evaluate the effects of the hydrocarbon layer residing near the homopause on ionospheric conductances, we performed two sets of calculations, with (solid curves) and without (dashed curves) a hydrocarbon layer (refer to Appendix A-2 in the Supporting Information S1 for more details).

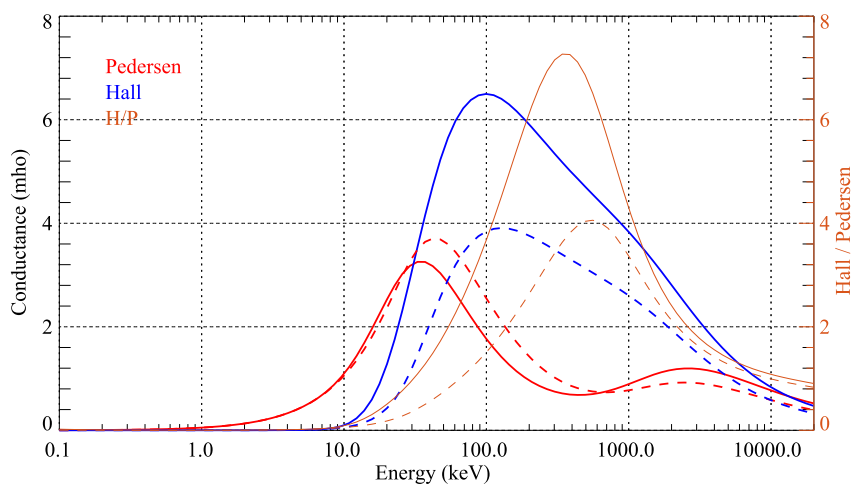

Figure 5. Calculated height-integrated Pedersen (red) and Hall (blue) conductivities (i.e., conductances) as functions of initial precipitating electron energy for a constant incident electron energy flux of 100 mW/m^2 and a magnetic field intensity of 10 G. The ratios of Hall to Pedersen conductance are shown as orange curves. Results with and without CH_4 included in the thermosphere are represented by solid and dashed curves, respectively.

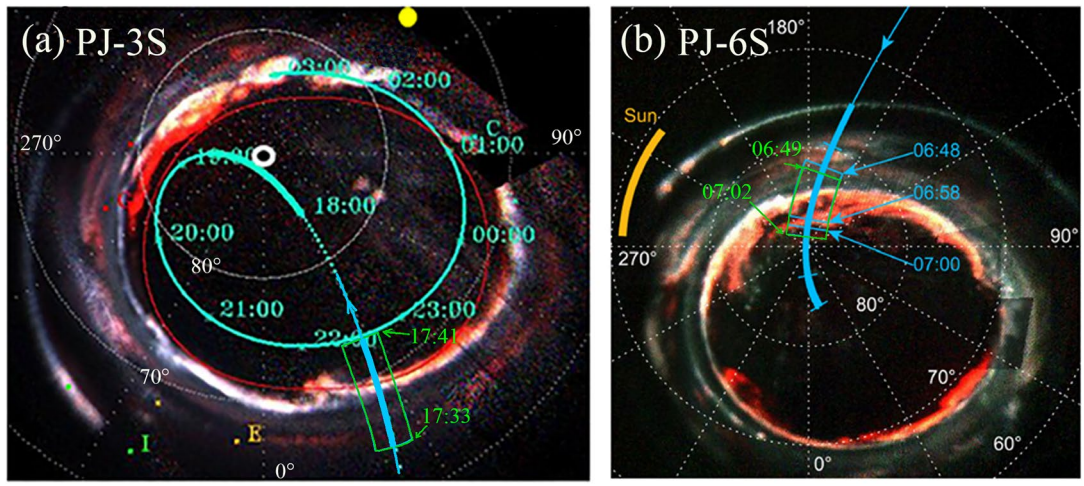

Figure 6. Polar projection of the ultraviolet (UV) aurora in false colors taken with the Juno UVS instrument during PJ-3S (a) and PJ-6S (b) in the left-handed System III coordinate system. The colors represent the brightness of different UV spectral bands, with red, green and blue tending to represent the high, medium and low energy electron precipitations (see Mauk et al., 2020). Overlaying the image is the magnetic footprint track of Juno, shown in light blue, calculated by using the JRM09 magnetic field model (Connerney et al., 2018) and the CAN81 current sheet model (Connerney et al., 1981). The time intervals displayed in Figures 7 and 8 correspond to the green boxes in each panel. The thick orange circle or arc shows the average direction to the Sun during the integration of the image. The UVS data shown in Panel (a) is adapted from Mauk et al. (2020), while panel (b) is adapted from Allegrini et al. (2020).

Solid curves represent the results with CH_4 included in the ionospheric chemical reactions with the vertical profile shown in Figure A1-1 of Appendix A-1 in the Supporting Information S1. Pedersen conductances (in red) display two peaks at energies of about 40 and 3,000 keV, respectively, separated by a minimum close to 500 keV. Conversely, Hall conductances display only one maximum around 100 keV. Hall conductances are larger than Pedersen conductances for all energies above approximately 20–30 keV. As analyzed in more detail in Appendix A-2 in the Supporting Information S1, the strong energy dependences of the two conductances and their ratios produce a modulation both in intensity and direction of horizontal ionospheric currents for a given ionospheric electric field.

Inclusion of CH_4 diminishes Pedersen conductances with respect to the case without CH_4 in an intermediate energy range (~30–~1,000 keV) and then increases them at higher energies. Both Hall conductances and the Hall/Pedersen conductance ratios are significantly enhanced when CH_4 is considered.

3.2. Detailed Analysis of Inputs and Key Parameters for PJ-3S and PJ-6S

In order to validate and illustrate our method to derive the key parameters of MIT coupling, we first choose two cases of main auroral oval crossing, PJ-3S and PJ-6S, for detailed analysis, and then present some statistical results for the eight selected southern perijoves. These two PJs correspond to two different local configurations of the main oval, as can be seen in Figure 6, which displays the UV brightness of the main oval measured by UVS: On the left (PJ-3S), the main oval is narrow in latitude, while on the right (PJ-6S) it is significantly extended in latitude and displays two separate regions of intense auroral emissions. It should be noted that these two time intervals correspond to dawn storms (Bonfond et al., 2021), however, these processes should not impact the dusk side of the magnetosphere, which is under study here. The time intervals of interest are highlighted by the green boxes in each panel.

Figure 7 shows the key MIT coupling parameters evaluated along Juno's trajectory during the auroral crossing for PJ-3S. As shown by Figure 6a, Juno crossed a relatively narrow main auroral oval during this southern polar cap fly-by, showing only one region of enhanced UV emission along its trajectory. The main auroral regions can be easily identified by the enhanced electron precipitation (panel (a)) and the strong magnetic-field-aligned currents (FACs) (panel (c)). The two FAC zones, that is, upward (blue shading) and downward (pink shading) appear to be contiguous, corresponding to the relatively narrow auroral oval shown in Figure 6a. An upward current is observed at colatitudes between 17.9° and 18.8° in magnetic coordinates, and a downward current sheet is seen just poleward of the upward one. An "inverted V"-like elec-

21699402, 2021, 9, Downloaded from https://agupubs.onlinelibrary.wiley.com/doi/10.1029/2021JA029469 by Cochraneltalia, Wiley Online Library on [26/02/2025]. See the Terms and Conditions (https://onlinelibrary.wiley.com/terms-and-conditions) on Wiley Online Library for rules of use; OA articles are governed by the applicable Creative Commons License

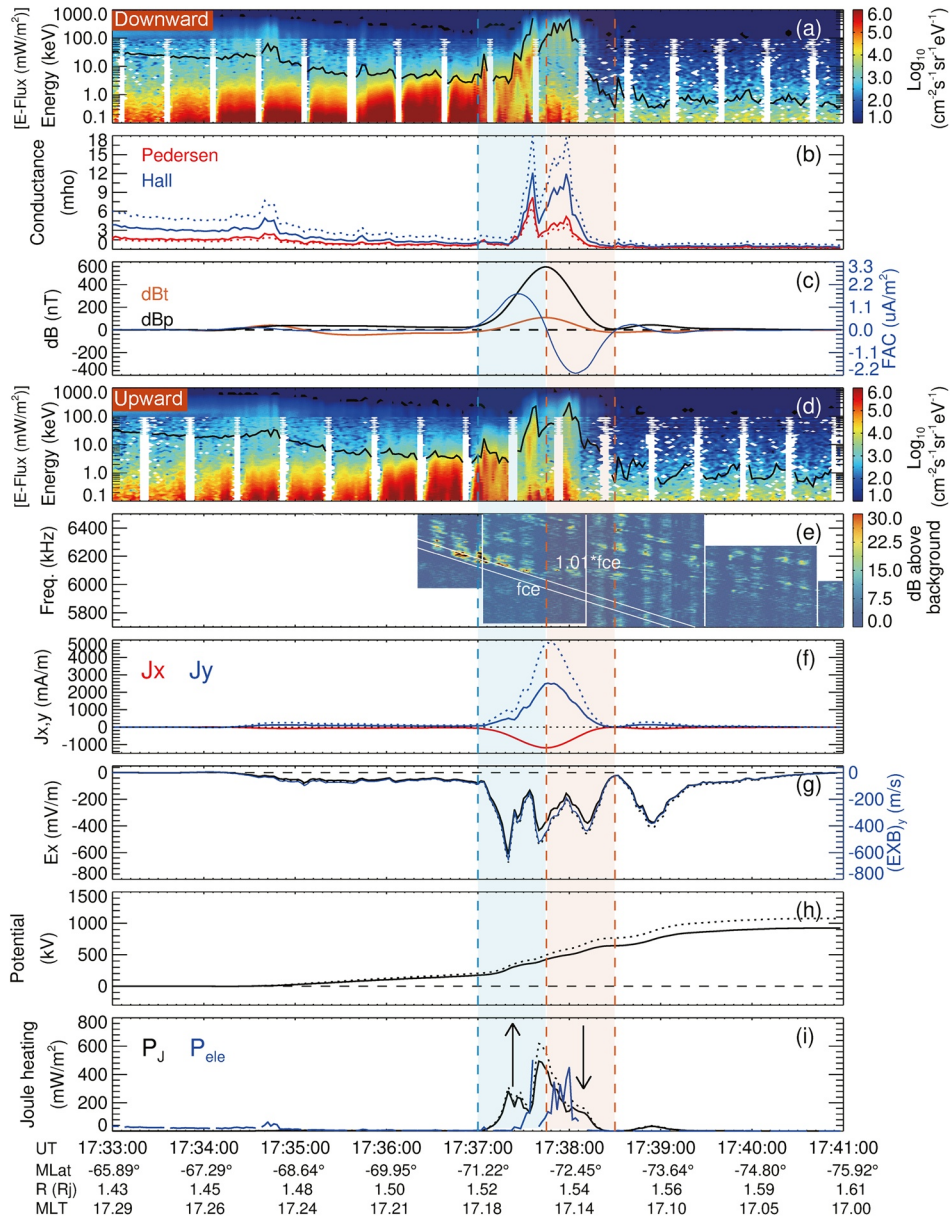

Figure 7. Time series of key parameters of $f_{ce} \times 1.01$ coupling versus time during the PJ-3S main auroral oval crossing. This eight-minute interval on December 11, 2016 during the southern perijove shows: (a) combined JADE and JEDI energy spectra for downward precipitating electrons. The black curve shows the total energy flux (mW/m^2) within the loss cone (the *y*-axis is the same as the energy scales in the left); (b) calculated height-integrated Pedersen (in red) and Hall conductivities (e.g., conductances) (in blue); (c) azimuthal magnetic perturbation δB_φ (black) and associated magnetic-field-aligned currents (FACs) calculated with our electrodynamics model; (d) Same as panel (a) but with upward electrons within the loss cone; (e) the burst mode Electric field Juno/Waves data. The two white lines indicate the local electron cyclotron frequency f_{ce} and $f_{ce} \times 1.01$, respectively; (f) Ionospheric height-integrated currents for the *x* and *y* components, where *x* and *y* are defined as perpendicular and parallel to the main oval (see Appendix A-3 in the Supporting Information S1 for more details); (g) *y* component of ionospheric electric field orthogonal to the local direction of the main auroral oval (continuous curve), overlaid with the *x* component (along the local direction of the oval) of the ionospheric E×B drift in the upper ionosphere; (h) electrostatic potential variation, assuming it goes to zero equatorward of the main oval, and (i) Joule and particle heating rates per unit column of atmosphere. The two vertical shadings indicate the main FAC current regions, blue for upward currents and pink for downward ones. The white blanks with a period of about 30s in the electron spectrum in panels (a) and (d) are caused by the breakdown of one of the three JADE sensors (e.g., Allegrini et al., 2017). Note that the dotted/solid curves in panel (b, f–i) show the results with/without including CH_4 in ionospheric chemical reactions. Data beneath panel (i) give the time (UT), magnetic latitude (deg), radial distance (R_J) and MLT (magnetic local time) of the spacecraft.

21699402, 2021, 9, Downloaded from https://agupubs.onlinelibrary.wiley.com/doi/10.1029/2021JA029469 by CochraneItalia, Wiley Online Library on [26/02/2025]. See the Terms and Conditions (https://onlinelibrary.wiley.com/terms-and-conditions) on Wiley Online Library for rules of use; OA articles are governed by the applicable Creative Commons License

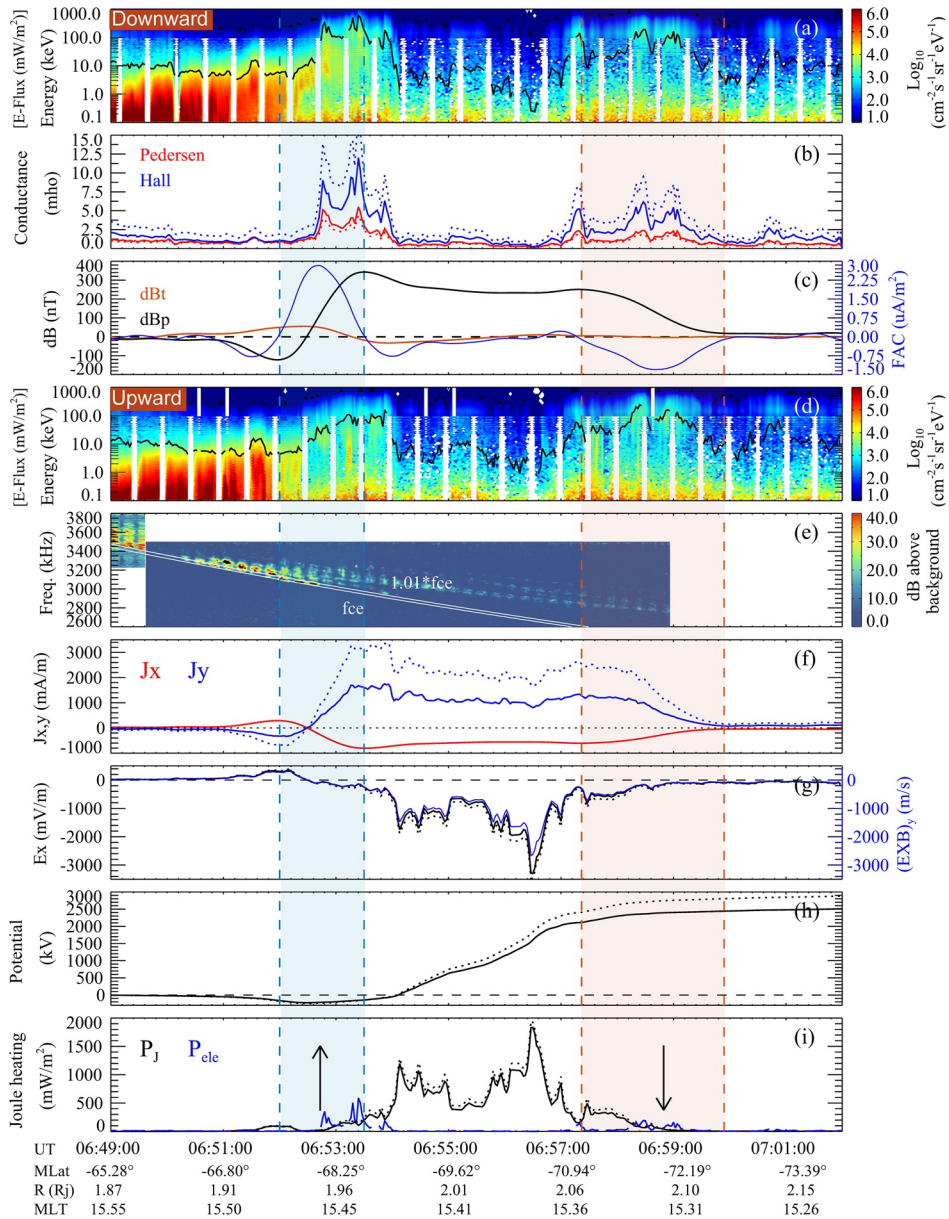

Figure 8. Key parameters of Magnetosphere-Ionosphere-Thermosphere coupling during PJ-6 main southern oval crossing on May 19, 2017. The captions are the same as in Figure 7.

tron distribution of downward precipitating electrons is observed in the upward current region (panel (a)), suggesting that electrons are accelerated via an upward electrostatic potential drop (e.g., Mauk et al., 2020). In addition, Waves data in panel (e) suggest that Juno flew inside a cyclotron-maser-instability (CMI) driven radio emission source between 17:36:44 and 17:37:36 UT, since the radio emission is mostly observed at frequencies lower than $f_{ce} \times 1.01$ (Louarn et al., 2018; Louis et al., 2019).

Auroral Pedersen and Hall conductance magnitudes vary over two orders of magnitude, from lower than 1 mho to over 10 mhos, across the main current regions, as a result of their modulation by electron precipitation (Figure 7, panels a and b). They are enhanced in these two auroral regions by a factor of over 5 with respect to their values in the adjacent regions. Hall conductances are 2–3 times higher than Pedersen conductances. Inclusion of CH_4 in the ionospheric chemical reactions slightly diminishes Pedersen conductances and strongly increases Hall conductances in comparison to the case without CH_4. As a result, the Pedersen-conductance controlled parameters (electric field E_x, electrical potential and Joule heating, as

21699402, 2021, 9, Downloaded from https://agupubs.onlinelibrary.wiley.com/doi/10.1029/2021JA029469 by CochraneItalia, Wiley Online Library on [26/02/2025]. See the Terms and Conditions (https://onlinelibrary.wiley.com/terms-and-conditions) on Wiley Online Library for rules of use; OA articles are governed by the applicable Creative Commons License

21699402, 2021, 9, Downloaded from https://agupubs.onlinelibrary.wiley.com/doi/10.1029/2021JA029469 by CochraneItalia, Wiley Online Library on [26/02/2025]. See the Terms and Conditions (https://onlinelibrary.wiley.com/terms-and-conditions) on Wiley Online Library for rules of use; OA articles are governed by the applicable Creative Commons License

shown in Figure 7, panels g–i, respectively) are almost unchanged, whereas the J_y current, which strongly depends on the Hall conductance, is largely enhanced due to the effect of CH_4. Electric field E_x and Joule heating are mainly enhanced within the FAC regions. A total potential drop on the order of 500 kV is found across the two main FAC sheets.

PJ-6S, our other case study, displays different FAC configurations in comparison to PJ-3S: Its upward and downward FAC zones are separated by a "zero FACs" latitude zone. This case has been studied in detail by Kotsiaros et al. (2019). As shown in Figure 6b, Juno's footprints first crossed the diffuse aurora equatorward of the main oval, and then the relatively discrete main oval followed by a secondary auroral patch. These two auroral regions can be recognized in the electron measurements shown in Figure 8a, where a strong enhancement of precipitation energy fluxes can be observed inside the auroral regions associated with each of the upward and downward FAC regions. Inside the main oval regions, FACs are mainly upward. In the second aurora patch, FACs are mainly downward, even though the downward electron precipitation is also intensified. Bidirectional beams are observed during these two auroral crossings.

Similar to PJ-3S, immediately equatorward of the main upward FAC region, Juno passed inside a radio emission source between 06:50:14 and 06:52:50 UT seen by Waves (Figure 8e) in coincidence with intense upward-going electrons (Figure 8d). Inspection of other PJs shows that this is a common phenomenon for southern perijoves: Equatorward of the main oval regions, an intensified radio emission source associated with upward electron beams can always be encountered, as previously reported by Louis et al. (2019). During the traverse of the radio emission region, bidirectional electron beams within the loss cone were observed with comparable total energy fluxes for upward/downward electrons (Louarn et al., 2018). Auroral Pedersen and Hall conductances (Figure 8b) display similar characteristics to the PJ-3S case.

Electric fields across the oval and Joule heating are low in the two main FAC regions, but reach their maxima in the region between them (Figure 8g). Within our calculation scheme, this is the result of the closure of these two FACs through a region of very low ionospheric conductances. The total electrostatic potential drop, on the order of 2.2 MV at ionospheric altitudes between the upward and downward FACs, can be estimated by integration of the electric field. The main voltage drop occurs in the region of low precipitation and low conductance in-between the two FAC sheets. However, since the Pedersen conductance, which is low in this region, comes as a divisor of J_x in the calculation of E_x (Equation A20 of Appendix A-3 in the Supporting Information S1), the uncertainty in this determination is large (see our discussion in Section 4.1).

The main FAC regions were observed at colatitudes between 16.9° and 18.8° for PJ-3S, with upward FAC equatorward of the downward FAC. As for PJ-6S, the upward FAC region lies at about 22.0° colatitude, while the downward one is about 18.0° in magnetic coordinates. Sub-corotation of the polar ionospheric plasma is evident in both cases as a systematic westward E×B plasma flow (panels g). Similar to the behaviors of FACs, these regions of westward E×B flows are mainly located within the adjacent FAC regions for PJ-3S, but in-between the two FACs for PJ-6S.

3.3. Statistical Study of the Eight Selected Southern Perijoves

To investigate the statistical characteristics of the key parameters of MIT coupling, we also analyzed the eight southern perijoves selected for further study (Table 3).

Distribution in Jupiter's rotating reference frame. Figure 9 shows the distributions in Orthographic polar projections of four parameters of MIT coupling in a reference frame rotating with Jupiter for the eight selected southern perijoves. These plots, using a right-hand magnetic dipole coordinate based on the dipole component of the JRM09 magnetic field model, show the Pedersen (a) and Hall (b) conductances and Joule heating rates per area of atmospheric column (c). Panel (d) shows the calculated sub-corotation rates, in fractions of Jupiter's planetary spin rate, with respect to the magnetic pole. In panels (a and b) the real-time main auroral oval location indicated by the local peak of the conductances (dark red) is not always located exactly at positions of the statistical main oval (shown with orange curves). Besides, high conductance magnitudes are also observed equatorward of the main oval. Joule-heating dominated regions (panel c) are mainly located in the vicinity and poleward of the main oval regions.

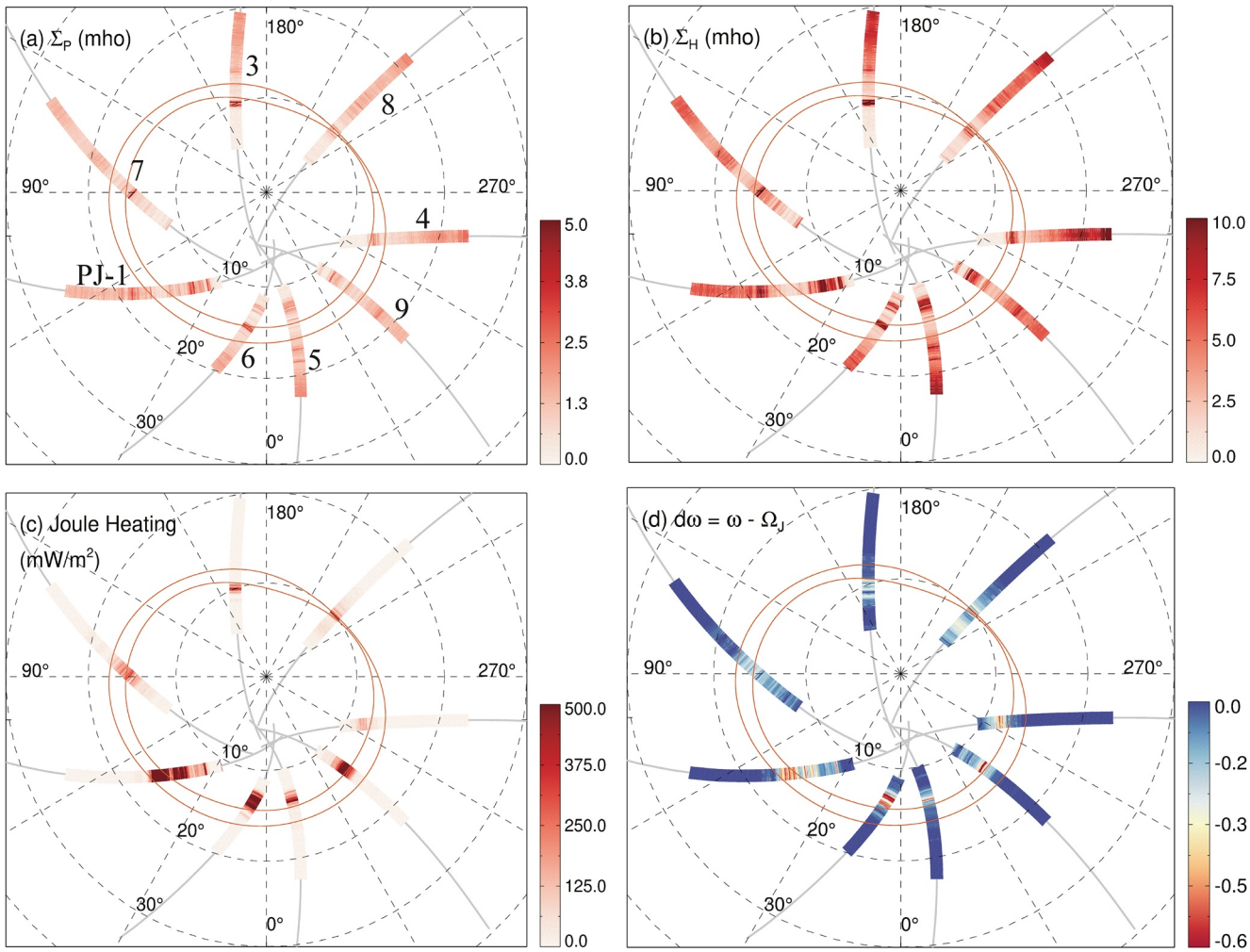

Figure 9. Orthographic polar projections of the key parameters of Magnetosphere-Ionosphere-Thermosphere coupling in a reference frame rotating with Jupiter, using right-hand magnetic dipole coordinates based on the dipole component of the JRM09 magnetic reference frame, for the eight selected southern perijoves. (a) Pedersen conductance, (b) Hall conductance, (c) Joule heating and (d) angular velocity of the ionospheric plasma, normalized to planetary rotation about the magnetic pole (which approximately corresponds to the center of the oval). The statistical main oval adapted from Bonfond et al. (2012) is plotted with orange curves for each panel. The magnetic colatitudes of 10°, 20°, 30° are also shown with dashed circles.

Panel (d) shows that subcorotation (in blue) is stronger near the main oval: $|d\omega|$ can reach up to 0.8 for some periods. This is consistent with the westward flow of the high-altitude ionospheric plasma observed for PJ-3S and even more for PJ-6S, for which the angular velocity of the plasma in the inertial frame deduced from E_x decreases to only 20% of planetary rotation.

Distribution in Magnetic Local time (MLT). Figure 10 shows the distribution of FACs (panel (a)) and of the normalized angular velocity of the ionospheric plasma (panel (b), same as panel (d) of Figure 9) relative to planetary rotation for the same eight southern perijoves. Juno, being mainly located on the dusk side, covered only local times between 14:00 and 18:00 during the eight selected perijoves. Westward plasma drifts (i.e., subcorotation) prevail for all perijoves, which are consistent with the predictions of the corotation-enforcement model, and also with observations of plasma flows in the dusk sector by Johnson et al. (2017). This local dominance of sub-corotating (westward and sunward) drifts in the dusk sector is also consistent with the global morphological model of high-latitude Jovian ionospheric plasma flows by Cowley et al. (2003), which is based on the interplay of "Hill-like" subcorotation with the Vasyliunas and Dungey convection cycles. It is also consistent in this same local time and magnetic latitude range with the model of Delamere and Bagenal (2010), in which the effects of a viscous-like interaction with the solar wind following Axford and Hines (1961) are superimposed to those of "Hill-like" subcorotation. Derivation of plasma flows and

21699402, 2021, 9, Downloaded from https://agupubs.onlinelibrary.wiley.com/doi/10.1029/2021JA029469 by CochraneItalia, Wiley Online Library on [26/02/2025]. See the Terms and Conditions (https://onlinelibrary.wiley.com/terms-and-conditions) on Wiley Online Library for rules of use; OA articles are governed by the applicable Creative Commons License

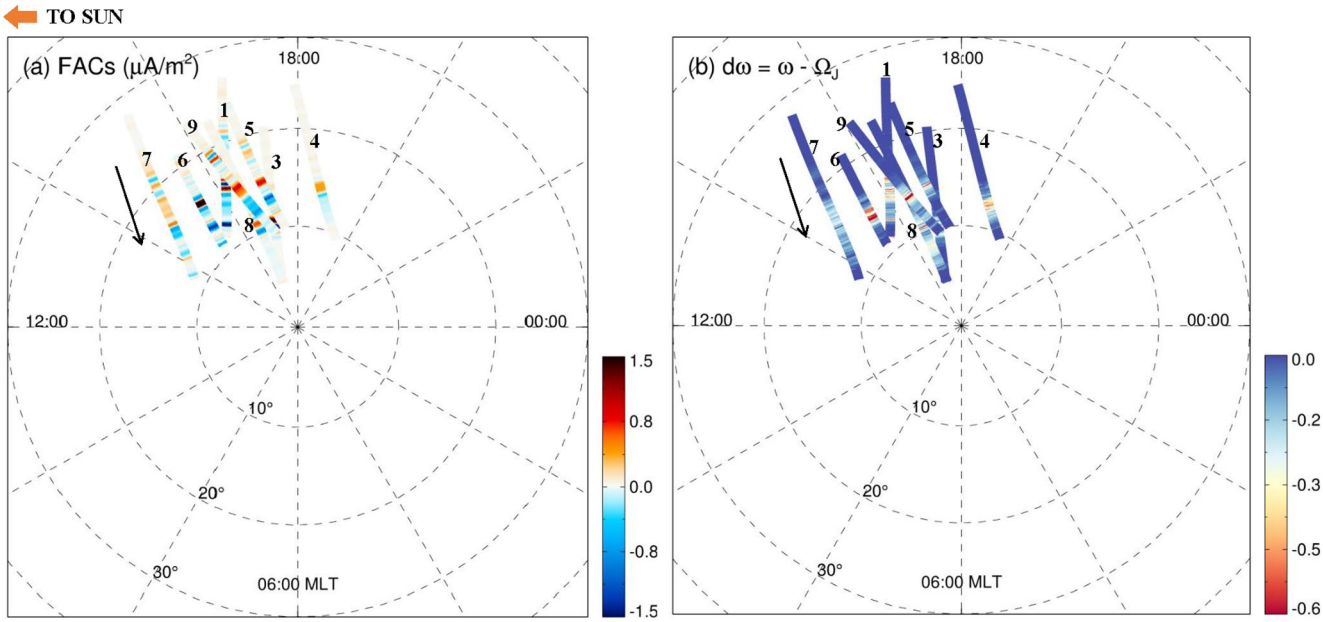

Figure 10. Magnetic Local time (MLT) versus magnetic latitude distribution of magnetic-field-aligned currents (a) and normalized angular velocities of the ionospheric plasma relative to planetary rotation around the magnetic pole (b) for the eight selected southern perijoves. 10°, 20° and 30° colatitude circles are also shown. The polar center in each panel represents the southern magnetic pole. The arrow in each panel indicates the direction of Juno's magnetic footprints.

other MIT coupling parameters at other local times and latitudes, using the longitude precession of Juno's orbit with time, will be mandatory to discriminate between the different types of plasma flow models.

4. Discussion

4.1. Degree of Robustness in the Derivation of MIT Coupling Parameters

To discuss the uncertainties associated with the derivation of the different key parameters, we will be guided by the flows of calculations summarized in Figure 4 and described in detail in the three appendices.

First (top arrow from MAG in Figure 4), both field-aligned current densities $J_{\|}$ and ionospheric currents orthogonal to the observed oval J_x are derived directly from the magnetic field variation δB measured by Juno and its derivative along its trajectory (Equations A12 and (A15) of Appendix 3 in the Supporting Information S1). This derivation relies solely on the assumption that variations of all quantities along the local auroral oval have much longer spatial scales than variations across the oval. Since we have chosen to study in detail auroral oval crossings for which this assumption holds based on the morphology of the UV aurora observed by UVS, the derivation of $J_{\|}$ and J_x is the most robust in our chain of calculations. Its uncertainty is on the order of the "smallness parameter" $\partial/\partial y/\partial/\partial x$. Besides, we checked that the calculation of these currents is also robust with respect to the choice of different internal magnetic field models such as JRM09 (Connerney et al., 2018) or VIP4 (Connerney et al., 1998).

Second, the derivation of ionospheric conductances $\Sigma_{P,H}$ (bottom part of Figure 4 starting from JADE and JEDI data) is directly dependent on the accuracy of electron precipitation energy spectra and pitch angle distribution derived from Juno and on the neutral atmosphere and ionosphere models. The accuracy of the neutral atmosphere and ionosphere models can be reasonably represented by the difference between the two ionosphere models we have used (with or without CH_4). One can see that the difference between the solid and dotted curves in the derivation of conductances in Figures 7 and 8 is on the order of 20%, an accuracy which seems sufficient to provide a relevant comparison with current models of MIT coupling. In addition, for a more comprehensive validation of the ionospheric model, a comparison of the modeled auroral UV/IR emissions (e.g., Tao et al., 2011) with UVS/JIRAM observations can be conducted in future studies.

21699402, 2021, 9, Downloaded from https://agupubs.onlinelibrary.wiley.com/doi/10.1029/2021JA029469 by Cochraneltalia, Wiley Online Library on [26/02/2025]. See the Terms and Conditions (https://onlinelibrary.wiley.com/terms-and-conditions) on Wiley Online Library for rules of use; OA articles are governed by the applicable Creative Commons License

21699402, 2021, 9, Downloaded from https://agupubs.onlinelibrary.wiley.com/doi/10.1029/2021JA029469 by Cochraneltalia, Wiley Online Library on [26/02/2025]. See the Terms and Conditions (https://onlinelibrary.wiley.com/terms-and-conditions) on Wiley Online Library for rules of use; OA articles are governed by the applicable Creative Commons License

Table 4
Ranges of Variation of Key MIT Coupling Parameters Provided by This Study Inside the Main Regions of FACs (Pink and Blue Vertical Bands of Figures 7 and 8) and by Our Statistical Study of the Eight Selected Perijoves

MIT coupling parameters	PJ-3S	PJ-6S	Statistical study
$\overrightarrow{J_{\parallel}}$ (μA/m^2)	[-2.1, 1.8]	[-1.3, 2.8]	[-1.2, 1.2]
J_x (mA/m)	[-1,185.16, 7.25]	[-803.89, 288.88]	[-747.9, 76.5]
Σ_P (mhos)	[0.2, 6.6]	[0.0, 4.4]	[0.1, 4.0]
Σ_H (mhos)	[0.6, 18.0]	[0.0, 18.1]	[0.3, 15.6]
J_y (mA/m)	[-25.7, 4,846.9]	[-693.0, 3,373.9]	[-219.3, 3,081.1]
E_x (mV/m)	[-674.7, 5.1]	[-3,507.1, 382.8]	[-1,723.0, 96.4]
P_{ele} (mW/m^2)	[0.3, 502.6]	[0.2, 591.0]	[0.3, 488.0]
P_J (mW/m^2)	[0, 617.8]	[0.4, 1,952.9]	[0.1, 1,098.6]

Third, the derivation of several other parameters uses the ionospheric Ohm's law (upper right corner of Figure 4), and is therefore directly sensitive to the accuracies in the determination of ionospheric conductance and sometimes to additional simplifying assumptions: (a) For the calculation of the electric current along the oval J_y, we neglected the neutral wind term in the Ohm's law, an assumption which is validated by current models of MIT coupling, as shown in Appendix A-3 in the Supporting Information S1. Under this approximation, J_y is directly proportional to J_x (Equation A23 in the Supporting Information S1) with a proportionality factor equal to Σ_H/Σ_P. The accuracy of its determination depends on how well our ionosphere model determines this ratio. (b) The two parameters, E_x and Q_J, are obtained via expressions in which J_x or J_θ are divided by Σ_P (equations A20 and A23 in the Supporting Information S1, respectively). For a constant error bar on Σ_P, which is a reasonable assumption, their uncertainty is inversely proportional to Σ_P: It is small when Σ_P is large, and large in the regions of low conductance, that is, mainly outside the pink and blue vertical bands in Figures 7 and 8 where the most intense FACs are concentrated.

4.2. Comparison With Previous Estimates of Ionospheric Conductances

Using the two-dimensional distribution of the electron energy flux and characteristic energy inferred from Juno UVS data, Gérard et al. (2020, 2021) calculated the Pedersen conductance for each UVS pixel to characterize the spatial distribution over auroral and polar regions within the UVS field of view and to investigate the hemispheric symmetry of the Pedersen conductance. Their calculated Pedersen conductances vary from less than 0.1 up to several mhos and maximize in the main aurora, high latitude precipitation, and Io magnetic footprint. The magnitudes of the calculated Pedersen conductance found in Gérard et al. (2020) are comparable to our results, although there are significant differences between our results and theirs. Using the same inputs of characteristic energy, energy flux and energy spectrum shape of the precipitating electrons as the ones used by Gérard et al. (2020) to derive conductances from the UVS data, we found nearly equal Pedersen conductances. Thus, the differences between the two results mainly come from the differences of electron precipitation energy spectra used in the two studies. Their values of the auroral electron flux and mean electron energy were derived from global UVS spectral images in contrast to the in-situ measurements used in this approach. In addition, Hall conductances are calculated only in our study.

4.3. Ranges and Major Trends of Derived MIT Coupling Parameters

Detailed analysis of perijoves PJ-3S and PJ-6S, together with a statistical study of the eight selected southern perijoves, provide preliminary estimates of the orders of magnitude (Table 4) and morphological features

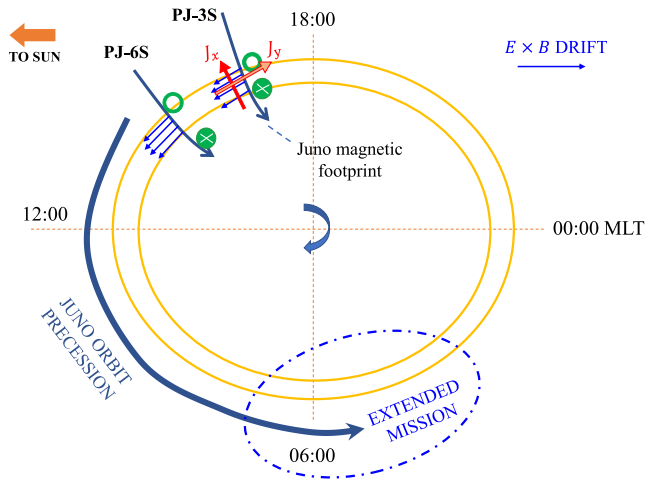

Figure 11. Schematic illustration of the main configuration of the ionospheric plasma flows and magnetic-field-aligned currents (FACs) for PJ-3S and PJ-6S in a reference frame centered on the magnetic pole. Orange circles represent the main ovals, and dark-blue curves show Juno magnetic footprints. Upward and downward FACs are shown with green circles and arrows, respectively. Red arrows indicate ionospheric currents J_x and J_y, while blue arrows represent the ionospheric E×B drifts. As time progresses, local time coverage of Juno observations will progressively extend (thick blue arrow) toward the dawn sector and beyond. The figure is viewed from the south pole and the sun is to the top.

of our derived MIT coupling parameters. These orders of magnitude are based only on data from the blue and pink vertical bands of Figure 7 (second column from left) for PJ-3S, of Figure 8 (third column from left) for PJ-6S, and on the median values found in our statistical analysis (right-hand-side column). Table 4 shows that the estimates of all parameters derived from PJ-3S, PJ-6S and the statistical study are mutually consistent.

The magnetic local time distribution of these parameters suggests a preliminary simplified description of the main configuration of ionospheric $\vec{E} \times \vec{B}$ plasma flows, FACs and horizontal ionospheric currents, shown in Figure 11. FACs are upward first within the main oval or near its equatorward edge, and then directed downward poleward of the oval. These two current sheets are either adjacent to each other (PJ-3S) or separated by a "zero-FAC" zone (PJ-6S). The ionospheric closure of these two oppositely directed FAC sheets produces equatorward horizontal ionospheric currents and electric fields whose ratio is controlled by the magnitude of the Pedersen conductance. The equatorward electric fields generated by the ionospheric current closure of FACs in turn drive an eastward ionospheric Hall current along the direction of the oval. Ionospheric plasma flows due to $\vec{E} \times \vec{B}$ convection are predominantly westward and opposite to the planet's rotation, producing sub-corotation of the ionospheric plasma as shown in Figure 10b. However, due to the limited MLT coverage of the sample of perijoves used, one cannot determine if this dominance of sub-corotation also prevails in other local time sectors, or varies with MLT, as for instance suggested by the observation of super-corotating flows from IR H_3^+ line redshift Earth-based observations by Johnson et al. (2017) in the dawn sector of the main oval. Since the orientation of Juno's orbit gradually precesses to the dawn sector and beyond as the mission progresses, using all orbits from the baseline mission and the extended mission will be critical to provide variations of ionospheric electric currents and plasma flows across a broad range of MLT that can be compared to model predictions.

4.4. Comparison With MHD Models and the Axisymmetric Corotation Enforcement Model

Jovian global magnetohydrodynamics (MHD) models can describe non-axisymmetric flows and include both planetary corotation enforcement and coupling to the solar wind in the same picture. In these models the ionosphere is usually simplified as a 2-dimensional layer with constant conductance (Sarkango et al., 2019; Zhang et al., 2018; Wang et al., 2018 and references therein) or as a virtual resistive layer coupled to the magnetosphere (e.g., Chané et al., 2013).

FACs in the ionosphere have been estimated by some of these modeling studies. In general, they find an upward current within the main oval regions, and a continuous downward current poleward of the oval. The peak current densities are about tens of nA/m^2, significantly weaker than the $\sim 1\ \mu A/m^2$ evaluated in this study. The total integrated outward current for each hemisphere amounts to about several MA, while, by integrating our local determinations of FACs along the Juno magnetic footprint across the width of the main upward currents and then extrapolating to the whole auroral oval, we estimate a total of 66 MA for the southern hemisphere from PJ-3S data (rather consistent with the estimates of Kotsiaros et al., 2019). This discrepancy may be due to the limits of the simplified ionosphere conductance models used in MHD simulations.

Using an axisymmetric model, Cowley et al. (2005, 2008; 2017) evaluated the MIT coupling parameters starting from a simple model of the ionospheric plasma angular flow. Their model for the normalized plasma angular velocity in the Jovian polar ionosphere is mainly composed of four regions with increasing colatitudes (see Figure S2 in Cowley et al., 2017). In region 1, from the pole to 10.72° colatitude, the ionospheric plasma strongly sub-corotates with a constant normalized angular velocity of 0.1. In region 2, up to 15.31°, its angular velocity is 0.35; in region 3, up to 17.33°, it increases sharply from 0.35 to 1.0. Finally, in region 4, rigid corotation prevails equatorward of 17.3°. The azimuth-integrated horizontal ionospheric

21699402, 2021, 9, Downloaded from https://agupubs.onlinelibrary.wiley.com/doi/10.1029/2021JA029469 by Cochraneltalia, Wiley Online Library on [26/02/2025]. See the Terms and Conditions (https://onlinelibrary.wiley.com/terms-and-conditions) on Wiley Online Library for rules of use; OA articles are governed by the applicable Creative Commons License

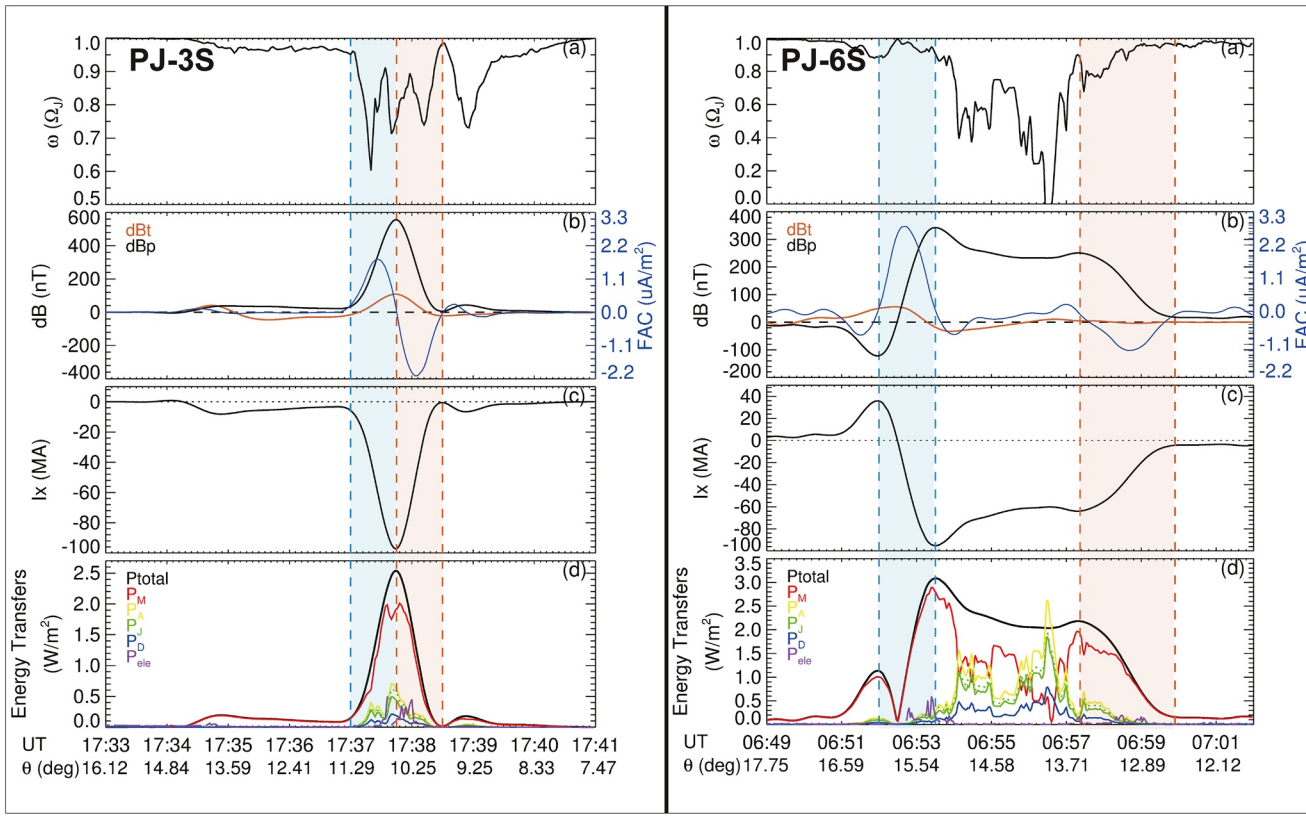

Figure 12. Temporal/colatitude variations of Magnetosphere-Ionosphere-Thermosphere coupling parameters for PJ-3S (left box) and PJ-6S (right box). (a) Plasma angular velocity normalized to the planetary angular velocity; (b) azimuthal magnetic perturbation δB_{φ} (black) and associated magnetic-field-aligned currentss; (c) azimuth-integrated meridional horizontal current $I_x\left(MA\right)$, positive poleward; (d) power transfer rates including $\left(P_{\text{total}}\right)$ the total power per unit area of atmosphere extracted from planetary rotation, $\left(P_M\right)$ power transferred to the magnetosphere, $\left(P_A\right)$ total dissipation as heat in the upper atmosphere, $\left(P_J\right)$ Joule heating, $\left(P_{\text{ele}}\right)$ electron precipitating energy flux, $\left(P_D\right)$ power transferred to subcorotation of the neutral atmosphere via ion drag. Data beneath panel (c) give the time (UT) and magnetic colatitude (deg) of the ionospheric footprints of the spacecraft.

current increases with colatitude from 0 to ~37 MA at the boundary between regions 1 and 2, drops there by ~8 MA due to the increase in plasma angular velocity, rises again to peak at ~54 MA near the boundary between regions 2 and 3, and then falls to zero across region 3 as the angular velocity rises to rigid corotation. Distributed downward FACs of ~55–80 nA/m^2 pervade regions 1 and 2, with narrow zones of upward FACs occurring between regions 1 and 2 and in region 3.

In Figure 12 we display our results in a format that allows an easier comparison with the models of Cowley et al. (2005, 2008; 2017). The magnetic footprints of the Juno spacecraft cross the main oval with decreasing colatitudes, providing a limited latitude coverage from about 7.5° to 16.1° for PJ-3S, and 12.1° to 17.8° for PJ-6S. As shown in panel b of Figure 12, our derived FAC peak current densities are on the order of ~1.0–2.0 $\mu A/m^2$, much higher than the ~0.4 $\mu A/m^2$ of Cowley et al. (2017)'s model. Our FAC distributions are also much more variable with latitude, as previously found in Kotsiaros et al. (2019). For example, in PJ-3S, FACs are mainly distributed near 11° colatitude with upward current and downward current adjacent to each other, and are almost zero at locations outside these regions where downward FACs are expected in Cowley et al. (2017)'s model. By extrapolating our local horizontal currents to all local times assuming azimuthal symmetry, we calculated azimuth-integrated meridional currents, shown in panel c, and found peak currents on the order of 100 MA, about twice the value in Cowley et al. (2017).

Cowley et al. (2005) defined a set of power transfer rates describing where energy extracted from planetary rotation is redistributed. Similarly, we calculated these terms from our data, by assuming azimuthal symmetry, and the results are shown in panel d of Figure 12.

21699402, 2021, 9, Downloaded from https://agupubs.onlinelibrary.wiley.com/doi/10.1029/2021JA029469 by CochraneItalia, Wiley Online Library on [26/02/2025]. See the Terms and Conditions (https://onlinelibrary.wiley.com/terms-and-conditions) on Wiley Online Library for rules of use; OA articles are governed by the applicable Creative Commons License

Among these power transfer rates, the total power per unit area of ionosphere extracted from planetary rotation$\left(P_{\text{total}}\right)$ is composed of the amount transferred to the magnetodisk to maintain its partial corotation $\left(P_M\right)$ and of dissipation as heat in the upper atmosphere $\left(P_A\right)$. P_A is the sum of two terms: The Joule heating rate $\left(P_J\right)$ and the power transferred to subcorotation of the neutral atmosphere due to the torque $\left(P_D\right)$.

For the calculation of these energy transfer terms, we introduced the three angular velocities defined by Cowley et al. (2005): The planet's angular velocity Ω_J, the angular velocity of the subcorotating plasma ω, and the angular velocity of the neutral atmosphere in the Pedersen layer Ω_J^*, which is expected to lie intermediate between ω and Ω_J due to the friction of ion-neutral collisions (Huang & Hill, 1989).

$$\Omega_J - \Omega_J^* = k\left(\Omega_J - \omega\right) \tag{1}$$

where k is between 0 and 1. For this comparison we set k to 0.3, similar to Tao et al. (2009). Under this assumption, the difference between the plasma angular velocity and the planet's rotation can be derived from the electric field as

$$\delta\omega = \Omega_J - \omega = \frac{E'_\theta}{\left(1-k\right)\rho B} \tag{2}$$

ρ is distance perpendicular to the magnetic axis, and B is the magnetic field at the Juno footprint. In this framework the total power per unit area of the ionosphere extracted from the planetary rotation is:

$$p = \Omega_J \cdot \rho B \cdot J_\theta \tag{3}$$

The fraction of the total power transferred to the magnetosphere via the magnetic field is

$$p_M = \omega \cdot \rho B \cdot J_\theta \tag{4}$$

The remaining power dissipated in the upper atmosphere is the sum of 2 terms: Joule heating rate P_A, and "ion drag" power p_D associated with the subcorotation of the neutral atmosphere:

$$p_D = p - p_M - p_J \tag{5}$$

In summary, the general orders of magnitudes of power transfer rates in Cowley et al.'s models that can be derived from our study are similar to the estimates of these models, and we also find a dominance of sub-corotation in the limited MLT region we observed, but our results show that MIT coupling at Jupiter is much more variable with latitude than in these models. This is not surprising considering that the Cowley et al.'s models assume a steady state and axisymmetric breakdown of corotation which cannot capture all aspects of a dynamic and non-axisymmetric system (see Bonfond et al., 2020).

4.5. Comparison With Ionospheric Measurements and Ionosphere-Thermosphere Models

Direct measurements of ionospheric parameters in the auroral and polar regions of Jupiter, particularly ion winds and temperatures, can be made from Earth using large aperture telescopes observing H_3^+ IR emissions. Stallard et al. (2001) produced H_3^+ ion line-of-sight velocities around the maximum of the H_3^+ IR emission from measurements of the Doppler shift of the H_3^+ $\nu 2$ Q(1,0) line at 3.953 μm. They used the high-resolution Cryogenic Echelle Spectrometer (CSHELL) on the NASA Infrared Telescope Facility (IRTF) on Mauna Kea, Hawaii, during the nights of September 7 to 11, 1998 (UT). More recently, following the same method, Johnson et al. (2017,; 2018) used the long-slit echelle spectrometer CRIRES instrument on ESO"s VLT to produce maps of line-of-sight H_3^+ ion velocities and ion temperatures over a broad field of view covering the northern polar cap in December 2012. These measurements are representative of ionospheric $\vec{E} \times \vec{B}$ drifts, as they prevail at altitudes well above the region of maximum ionospheric conductivities where ion-neutral collisions are negligible and both ions and electrons are fully magnetized. The component of the measured $\vec{E} \times \vec{B}$ drifts along the local direction of the main oval can be therefore directly compared to our estimates (panels g of Figures 7 and 8). Stallard et al.'s velocity profiles are consistent with an ion wind of ~1.2 km/s to 1.5 km/s flowing clockwise along the main northern oval, that is, in the direction opposite to planetary rotation, for the night of September 11, and with somewhat lower velocities for September 8 and 10. Johnson et al.'s measurements cover a variety of situations, with weak sub-corotation flows in the dusk

21699402, 2021, 9, Downloaded from https://agupubs.onlinelibrary.wiley.com/doi/10.1029/2021JA029469 by Cochraneltalia, Wiley Online Library on [26/02/2025]. See the Terms and Conditions (https://onlinelibrary.wiley.com/terms-and-conditions) on Wiley Online Library for rules of use; OA articles are governed by the applicable Creative Commons License

21699402, 2021, 9, Downloaded from https://agupubs.onlinelibrary.wiley.com/doi/10.1029/2021JA029469 by Cochraneltalia, Wiley Online Library on [26/02/2025]. See the Terms and Conditions (https://onlinelibrary.wiley.com/terms-and-conditions) on Wiley Online Library for rules of use; OA articles are governed by the applicable Creative Commons License

sectors and both stronger sub-corotation and super-corotation flows at and slightly equatorward of the main oval, respectively, in the dawn sector. Their measured line-of-sight drifts are in the range of 0.5– to 2.5 km/s, depending on location. Comparison with our estimates of ion $\vec{E} \times \vec{B}$ winds is not fully relevant since their measurements were made for the northern polar cap, but if we convert our estimated E_x into an $\vec{E} \times \vec{B}$ drift given the local magnetic field magnitude ($\sim 10G$), its typical value of 400 mV/m is significantly lower than the largest ion winds observed by Johnson et al. (2017) in the dawn sector. However, our ion wind estimates correspond to the afternoon-to-dusk sector (see Figures 10 and 11). Therefore, they can be best compared to the weak sub-corotating flows they observed in the dusk sector, which display intensities in the 0.5– to 1 km/s range, reasonably consistent with our estimates based on field-aligned closure calculations.

Existing 3D models of the response of the Jovian thermosphere to auroral momentum and energy deposition provide useful figures to be compared to our estimates of FACs, ion winds and energy deposition rates, despite the fact that they generally describe different situations.

In their Jovian Ionosphere Model (JIM) study, Millward et al. (2002) simulated the response of the ionosphere and thermosphere to auroral energy deposition by 10 keV electrons with an average energy flux of 70 mW/m^2 in the main oval region. They found Pedersen conductances on the order of 0.25 mhos, significantly lower than our estimate, knowing that their assumed characteristic precipitating electron energy is also significantly lower than what we observe with Juno.

Using their Jupiter Thermosphere General Circulation Model (JTGCM), Bougher et al. (2005) introduced forcing sources due to the auroral ionosphere (energetic particle precipitation, ion drag, Joule heating) with the main purpose of assessing their contribution to the global energy balance of the thermosphere. They found these high-latitude sources to be of prime importance to fit Galileo probe data. Among the three cases they studied, the inputs and outputs for Case 2 (intermediate intensity auroral heating) give a column-integrated total auroral energy input of 140 mW/m^2, a particle energy deposition rate of 8.5 mW/m^2, and a Pedersen conductance on the order of 10 mhos in the southern main auroral circle, comparable to our estimates of MIT coupling parameters.

Finally, the axisymmetric 2D simulation study of MIT coupling by Tao et al. (2009) offers probably the most relevant results to compare with our estimates. In their simulation, transfer of angular momentum between the ionosphere and the magnetodisk is self-consistently coupled to a dynamic thermosphere set into motion by ion drag and Joule heating. Their distribution of FACs, with two adjacent current sheets flowing upward (on the equatorial edge) and downward (on the polar edge) over a 2° latitude range centered around 73° latitude, is morphologically similar to our PJ-3S case study. Both their maximum Pedersen conductance (0.75 mhos) and FAC intensity (0.5 mA/m^2) are an order of magnitude smaller than our estimates. In contrast, their total power inputs to the thermosphere, 200– to 300 mW/m^2, are remarkably consistent with our estimates of P_J. In their model, ion drag and Joule heating combine to produce a sub-corotation of the thermosphere and a meridional cell of neutral air driving moderate intensity winds and large intensity westward winds equatorward of the FAC regions. As these winds reach significant intensities only above the altitudes where conductivities maximize, they effectively transport angular momentum stored in thermospheric planetary rotation equatorward of the main oval, but without a significant effect on the auroral current systems and on the atmosphere layers within which these currents flow.

In summary, comparison of our MIT coupling parameter estimates with the limited number of available models and observations is made difficult by the very large spatial and temporal variability of the Jovian auroral ionosphere. Producing significant comparisons will require a more direct interplay between observations and models.

5. Summary and Conclusions

In this study, we proposed a new method combining Juno multi-instrument data and modeling tools to derive several key parameters of MIT coupling at Jupiter along Juno's ionospheric magnetic footprint: FAC and ionospheric horizontal electric currents, Pedersen and Hall ionospheric conductances, electric fields, Joule and particle energy deposition into the upper atmosphere. Electron, magnetic field, waves and UV

21699402, 2021, 9, Downloaded from https://agupubs.onlinelibrary.wiley.com/doi/10.1029/2021JA029469 by Cochraneltalia, Wiley Online Library on [26/02/2025]. See the Terms and Conditions (https://onlinelibrary.wiley.com/terms-and-conditions) on Wiley Online Library for rules of use; OA articles are governed by the applicable Creative Commons License

imaging Juno data were used as inputs to three models, a Jovian atmospheric model, an ionospheric model and an electrodynamics model, to calculate these key parameters.

To validate our method, we studied two representative cases, PJ-3S and PJ-6S, before performing a statistical analysis of eight southern auroral zone crossings. These two cases correspond to two distinct configurations of the FAC latitude variations across the main south oval. In the first one (PJ-3S), upward and downward FAC regions are adjacent to each other and the main subcorotation and energy dissipation regions are located within the FAC regions. In the second one (PJ-6S) they are separated by a "zero-FAC" latitude zone and the main dissipation regions occur in the "zero-FAC" latitude zone between them.

Based on these studies, the key parameters of MIT coupling appear highly variable throughout Juno's auroral crossings. Electron precipitations strongly enhance ionospheric conductances in the main oval regions, where upward and downward FACs are intensified. Auroral Pedersen and Hall conductances are highly variable, ranging from lower than 1 mho to over 10 mhos. Peak FACs alternate from about −2 to 2 $\mu A/m^2$ during the traverses of the main aurora. Hall conductances are usually 2–3 times larger than Pedersen conductances, similarly to the Earth case.

A preliminary analysis of the budget of energy transfer between planetary rotation, the magnetodisk and high-latitude thermosphere using the modeling assumptions of Cowley et al. (2005) indicates that the total power per unit area of atmosphere extracted from planetary rotation can reach up to ∼3 W/m^2 in some cases. Joule heating dominates the power dissipated in the atmosphere and can be as large as ∼1.0 W/m^2. A brief comparison with predictions of Cowley et al. (2005, 2008; 2017)'s model showed that our calculated MIT coupling parameters display more complex and less regular variations. The directions of ionospheric E ×B drifts are generally consistent with the subcorotation predicted by these models in the dusk-to-afternoon MLT sector. Measurements made in different local time sectors taking advantage of the precession of Juno's orbit through noon and toward the morning sector will be critical to determine whether sub-corotation prevails at other local times and what could be the contributions of other flow systems, such as the Vasyliunas and Dungey cycles (Cowley et al., 2003) or a viscous-like interaction with the solar wind as suggested by Delamere and Bagenal (2010), to the global high-latitude flow pattern.

Although our method is able to evaluate the main parameters involved in MIT coupling, there are significant areas for improvements. First, in our current ionospheric model, the calculation of the ionization rate does not include the effects of the solar EUV radiation. In addition, we only studied eight southern perijoves and will extend our work in the near future to a larger set of Juno orbits, including the northern perijoves, to progressively build a comprehensive view of MIT coupling at Jupiter. Due to its orbit configuration, Juno was limited near the dusk side during the eight perijoves we studied. As time progresses toward its extended mission, Juno's orbit progressively scans earlier local times, thus potentially allowing our method to unravel the MLT dependence of electric currents, fields and plasma flows at ionospheric latitudes over the two polar caps.

Acknowledgments
We are very grateful to NASA and to the contributing institutions that have made the Juno mission possible, and to all institutions supporting the development, operation and data analysis of the Juno instrument suite used in this study: MAG, UVS, JIRAM, JADE, JEDI, Waves. Special thanks to John E. Connerney, Principal Investigator of the MAG experiment and to the MAG team for their critical support to this study. The French authors wish to express their gratitude to CNES for its support to their participation in the Juno mission. Y.X. Wang and C. Wang were supported by the Strategic Priority Research Program of Chinese Academy of Sciences grant Nos. XDB 41000000, NNSFC grants 41731070 and CAS grants QYZDJ-SSW-JSC028. B. Bonfond is a Research Associate of the Belgian Fonds de la Recherche Scientifique-FNRS. J.-C. Gérard, B. Bonfond, and D. Grodent acknowledge financial support from the Belgian Federal Science Policy Office (BELSPO) via the PRODEX Program of ESA.

Data Availability Statement

All Juno data used in this study are archived and available in NASA's Planetary Data System (https://pds.jpl.nasa.gov) and, for particles-and-fields data, in the CDPP (http://amda.cdpp.eu/, CNES- CNRS). All the data and codes used in our method are available at National Space Science Data Center (https://dx.doi.org/10.12176/01.99.00375) as shown in the in-text data citation reference: Wang et al. (2021).

References

Adriani, A., Filacchione, G., Di Iorio, T., Turrini, D., Noschese, R., Cicchetti, A., et al. (2017). JIRAM, the Jovian infrared auroral mapper. *Space Science Reviews*, *213*(1–4), 393–446. https://doi.org/10.1007/s11214-014-0094-y

Adriani, A., Mura, A., Moriconi, M. L., Dinelli, B. M., Fabiano, F., Altieri, F., et al. (2017). Preliminary JIRAM results from Juno polar observations: 2. Analysis of the Jupiter southern H_3^+ emissions and comparison with the north aurora. *Geophysical Research Letters*, *44*, 4633–4640. https://doi.org/10.1002/2017GL072905

Allegrini, F., Bagenal, F., Bolton, S., Connerney, J., Clark, G., Ebert, R. W., et al. (2017). Electron beams and loss cones in the auroral regions of Jupiter. *Geophysical Research Letters*, *9*, 7131–7139. https://doi.org/10.1002/2017gl073180

Allegrini, F., Mauk, B., Clark, G., Gladstone, G. R., Hue, V., Kurth, W. S., et al. (2020). Energy flux and characteristic energy of electrons over Jupiter's main auroral emission. *Journal of Geophysical Research: Space Physics*, *125*(4), e2019JA027693. https://doi.org/10.1029/2019ja027693

Axford, W. I., & Hines, C. O. (1961). A unifying theory of high latitude geophysical phenomena and geomagnetic storms. *Canadian Journal of Physics*, *39*, 1433–1464. https://doi.org/10.1139/p61-172

Bagenal, F., Adriani, A., Allegrini, F., Bolton, S. J., Bonfond, B., Bunce, E. J., et al. (2017). Magnetospheric science objectives of the Juno mission. *Space Science Reviews*, *213*(1–4), 219–287. https://doi.org/10.1007/s11214-014-0036-8

Bagenal, F., & Delamere, P. A. (2011). Flow of mass and energy in the magnetospheres of Jupiter and Saturn. *Journal of Geophysical Research*, *116*(A5), A05209. https://doi.org/10.1029/2010ja016294

Banks, P. M., & Kockarts, G. (1973). *Aeronomy*. Academic Press.

Bigg, E. K. (1964). Influence of the satellite Io on Jupiter's decametric emission. *Nature*, *203*(4949), 1008–1010. https://doi.org/10.1038/2031008a0

Blelly, P.-L., Marchaudon, A., Indurain, M., Witasse, O., Amaya, J., Chide, B., et al. (2019). Transplanet: A web service dedicated to modeling of planetary ionospheres. *Planetary and Space Science*, *169*, 35–44. https://doi.org/10.1016/j.pss.2019.02.008

Bolton, S. J., Bagenal, F., Blanc, M., Cassidy, T., Chané, E., Jackman, C., et al. (2015). Jupiter's magnetosphere: Plasma sources and transport. *Space Science Reviews*, *192*(1–4), 209–236. https://doi.org/10.1007/s11214-015-0184-5

Bolton, S. J., Lunine, J., Stevenson, D., Connerney, J. E. P., Levin, S., Owen, T. C., et al. (2017). The Juno mission. *Space Science Reviews*, *213*(1–4), 5–37. https://doi.org/10.1007/978-94-024-1560-5_2

Bonfond, B., Grodent, D., Gérard, J.-C., Stallard, T., Clarke, J. T., Yoneda, M., et al. (2012). Auroral evidence of Io's control over the magnetosphere of Jupiter. *Geophysical Research Letters*, *39*, L01105. https://doi.org/10.1029/2011gl050253

Bonfond, B., Yao, Z., & Grodent, D. (2020). Six pieces of evidence against the corotation enforcement theory to explain the main aurora at Jupiter. *Journal of Geophysical Research: Space Physics*, *125*, e2020JA028152. https://doi.org/10.1029/2020JA028152

Bonfond, B., Yao, Z. H., Gladstone, G. R., Grodent, D., Gérard, J. C., Matar, J., et al. (2021). Are dawn storms Jupiter's auroral substorms? *AGU Advances*, *2*, e2020AV000275. https://doi.org/10.1029/2020av000275

Bougher, S. W., Waite, J. H., Jr, Majeed, T., Gladstone, G. R. (2005). Jupiter Thermospheric General Circulation Model (JTGCM): Global structure and dynamics driven by auroral and Joule heating. *Journal of Geophysical Research*, *110*(E4), E04008. https://doi.org/10.1029/2003je002230

Broadfoot, A. L., Belton, M. J., Takacs, P. Z., Sandel, B. R., Shemansky, D. E., Holberg, J. B., et al. (1979). Extreme ultraviolet observations from voyager 1 encounter with Jupiter. *Science*, *204*(4396), 979–982. https://doi.org/10.1126/science.204.4396.979

Burke, B. F., & Franklin, K. L. (1955). Observations of a variable radio source associated with the planet Jupiter. *Journal of Geophysical Research*, *60*(2), 213–217. https://doi.org/10.1029/jz060i002p00213

Chané, E., Saur, J., & Poedts, S. (2013). Modeling Jupiter's magnetosphere: Influence of the internal sources. *Journal of Geophysical Research: Space Physics*, *118*(5), 2157–2172. https://doi.org/10.1002/jgra.50258

Clarke, J. T., Ballester, G., Trauger, J., Ajello, J., Pryor, W., Tobiska, K., et al. (1998). Hubble Space Telescope imaging of Jupiter's UV aurora during the Galileo orbiter mission. *Journal of Geophysical Research*, *103*(E9), 20217–20236. https://doi.org/10.1029/98JE01130

Connerney, J. E. P., Acuña, M. H., & Ness, N. F. (1981). Modeling the Jovian current sheet and inner magnetosphere. *Journal of Geophysical Research*, *86*(A10), 8370–8384. https://doi.org/10.1029/ja086ia10p08370

Connerney, J. E. P., Acuña, M. H., Ness, N. F., & Satoh, T. (1998). New models of Jupiter's magnetic field constrained by the Io flux tube footprint. *Journal of Geophysical Research*, *103*, 11929–11939. https://doi.org/10.1029/97ja03726

Connerney, J. E. P., Benn, M., Bjarno, J. B., Denver, T., Espley, J., Jorgensen, J. L., et al. (2017). The Juno magnetic field investigation. *Space Science Reviews*, *213*(1–4), 39–138. https://doi.org/10.1007/978-94-024-1560-5_6

Connerney, J. E. P., Kotsiaros, S., Oliversen, R. J., Espley, J. R., Joergensen, J. L., Joergensen, P. S., et al. (2018). A new model of Jupiter's magnetic field from Juno's first nine orbits. *Geophysical Research Letters*, *45*(6), 2590–2596. https://doi.org/10.1002/2018GL077312

Cowley, S. W. H., Alexeev, I. I., Belenkaya, E. S., Bunce, E. J., Cottis, C. E., Kalegaev, V. V., et al. (2005). A simple axisymmetric model of magnetosphere-ionosphere coupling currents in Jupiter's polar ionosphere. *Journal of Geophysical Research*, *110*(A11), A11209. https://doi.org/10.1029/2005ja011237

Cowley, S. W. H., & Bunce, E. J. (2001). Origin of the main auroral oval in Jupiter's coupled magnetosphere-ionosphere system. *Planetary and Space Science*, *49*(10–11), 1067–1088. https://doi.org/10.1016/s0032-0633(00)00167-7

Cowley, S. W. H., Bunce, E. J., Stallard, T. S., & Miller, S. (2003). Jupiter's polar ionospheric flows: Theoretical interpretation. *Geophysical Research Letters*, *30*(5), 1220. https://doi.org/10.1029/2002gl016030

Cowley, S. W. H., Deason, A. J., & Bunce, E. J. (2008). Axi-symmetric models of auroral current systems in Jupiter's magnetosphere with predictions for the Juno mission. *Annales Geophysicae*, *26*(12), 4051–4074. https://doi.org/10.5194/angeo-26-4051-2008

Cowley, S. W. H., Provan, G., Bunce, E. J., & Nichols, J. D. (2017). Magnetosphere-ionosphere coupling at Jupiter: Expectations for Juno Perijove 1 from a steady state axisymmetric physical model. *Geophysical Research Letters*, *44*(10), 4497–4505. https://doi.org/10.1002/2017gl073129

Delamere, P. A., & Bagenal, F. (2010). Solar wind interaction with Jupiter's magnetosphere. *Journal of Geophysical Research*, *115*, A10201. https://doi.org/10.1029/2010JA015347

Dinelli, B. M., Fabiano, F., Adriani, A., Altieri, F., Moriconi, M. L., Mura, A., et al. (2017). Preliminary JIRAM results from Juno polar observations: 1. Methodology and analysis applied to the Jovian northern polar region. *Geophysical Research Letters*, *44*, 10–4632. https://doi.org/10.1002/2017GL072929

Drossart, P., Maillard, J., Caldwell, J., Kim, S., Watson, J., Majewski, W., et al. (1989). Detection of H_3^+ on Jupiter. *Nature*, *340*, 539–541. https://doi.org/10.1038/340539a0

Elliott, S. S., Sulaiman, A. H., Kurth, W. S., Faden, J., Allegrini, F., Valek, P., et al. (2021). The high-latitude extension of Jupiter's Io torus: Electron densities measured by Juno Waves. *Journal of Geophysical Research: Space Physics*, *126*, e2021JA029195. https://doi.org/10.1029/2021ja029195

Gérard, J.-C., Bonfond, B., Grodent, D., Radioti, A., Clarke, J. T., Gladstone, G. R., et al. (2014). Mapping the electron energy in Jupiter's aurora: Hubble spectral observations. *Journal of Geophysical Research: Space Physics*, *119*, 9072–9088. https://doi.org/10.1002/2014JA020514

Gérard, J.-C., Bonfond, B., Mauk, B. H., Gladstone, G. R., Yao, Z. H., Greathouse, T. K., et al. (2019). Contemporaneous observations of Jovian energetic auroral electrons and ultraviolet emissions by the Juno spacecraft. *Journal of Geophysical Research: Space Physics*, *124*(11), 8298–8317. https://doi.org/10.1029/2019ja026862

21699402, 2021, 9, Downloaded from https://agupubs.onlinelibrary.wiley.com/doi/10.1029/2021JA029469 by CochraneItalia, Wiley Online Library on [26/02/2025]. See the Terms and Conditions (https://onlinelibrary.wiley.com/terms-and-conditions) on Wiley Online Library for rules of use; OA articles are governed by the applicable Creative Commons License

Gérard, J.-C., Gkouvelis, L., Bonfond, B., Grodent, D., Gladstone, G. R., Hue, V., et al. (2020). Spatial distribution of the Pedersen conductance in the Jovian aurora from Juno-UVS spectral images. *Journal of Geophysical Research: Space Physics*, *125*, e2020JA028142. https://doi.org/10.1029/2020ja028142

Gérard, J.-C., Gkouvelis, L., Bonfond, B., Grodent, D., Gladstone, G. R., Hue, V., et al. (2021). Variability and hemispheric symmetry of the Pedersen conductance in the Jovian aurora. *Journal of Geophysical Research: Space Physics*, 126. e2020JA028949. https://doi.org/10.1029/2020ja028949

Gershman, D. J., Connerney, J. E. P., Kotsiaros, S., DiBraccio, G. A., Martos, Y. M., -Viñas, F. A., et al. (2019). Alfvénic fluctuations associated with Jupiter's auroral emissions. *Geophysical Research Letters*, *46*, 7157–7165. https://doi.org/10.1029/2019GL082951

Gladstone, G. R., Persyn, S. C., Eterno, J. S., Walther, B. C., Slater, D. C., Davis, M. W., et al. (2017). The Ultraviolet Spectrograph on NASA's Juno Mission. *Space Science Reviews*, *213*(1–4), 447–473. https://doi.org/10.1007/s11214-014-0040-z

Gladstone, G. R., Waite, J. H., & Lewis, W. S. (1998). Secular and local time dependence of Jovian X ray emissions. *Journal of Geophysical Research*, *103*(E9), 20083–20088. https://doi.org/10.1029/98je00737

Grodent, D. (2015). A Brief Review of Ultraviolet Auroral Emissions on Giant Planets. *Space Science Reviews*, *187*(1–4), 23–50. https://doi.org/10.1007/978-1-4939-3395-2_3

Grodent, D., Bonfond, B., Yao, Z., Gérard, J.-C., Radioti, A., Dumont, M., et al. (2018). Jupiter's aurora observed with HST during Juno orbits 3 to 7. *Journal of Geophysical Research: Space Physics*, *123*, 3299–3319. https://doi.org/10.1002/2017JA025046

Grodent, D., Waite, J. H., & Gérard, J.-C. (2001). A self-consistent model of the Jovian auroral thermal structure. *Journal of Geophysical Research*, *106*(A7), 12933–12952. https://doi.org/10.1029/2000ja900129

Gurnett, D. A., Shawhan, S. D., & Shaw, R. R. (1983). Auroral hiss, Z mode radiation, and auroral kilometric radiation in the polar magnetosphere : DE 1 observations. *Journal of Geophysical Research*, *88*, 329–340. https://doi.org/10.1029/ja088ia01p00329

Hill, T. W. (2001). The Jovian auroral oval. *Journal of Geophysical Research*, *106*(A5), 8101–8107. https://doi.org/10.1029/2000JA000302

Hiraki, Y., & Tao, C. (2008). Parameterization of ionization rate by auroral electron precipitation in Jupiter. *Annales Geophysicae*, *26*(1), 77–86. https://doi.org/10.5194/angeo-26-77-2008

Huang, T. S., & Hill, T. W. (1989). Corotation lag of the Jovian atmosphere, ionosphere, and magnetosphere. *Journal of Geophysical Research*, *94*(A4), 3761. https://doi.org/10.1029/ja094ia04p03761

Johnson, R. E., Melin, H., Stallard, T. S., Tao, C., Nichols, J. D., & Chowdhury, M. N. (2018). Mapping H_3^+ temperatures in Jupiter's northern auroral ionosphere using VLT-CRIRES. *Journal of Geophysical Research: Space Physics*, *123*, 5990–6008. https://doi.org/10.1029/2018JA025511

Johnson, R. E., Stallard, T. S., Melin, H., Nichols, J. D., & Cowley, S. W. H. (2017). Jupiter's polar ionospheric flows: High resolution mapping of spectral intensity and line-of-sight velocity of H_3^+ ions. *Journal of Geophysical Research: Space Physics*, *122*, 7599–7618. https://doi.org/10.1002/2017JA024176

Khurana (2001). Influence of solar wind on Jupiter's magnetosphere deduced from currents in the equatorial plane. *Journal of Geophysical Research*, *106*(A11), 25999–26016. https://doi.org/10.1029/2000ja000352

Kivelson, M. G., Bagenal, F., Kurth, W. S., Neubauer, F. M., Paranicas, C., & Saur, J. (2004). Magnetospheric interactions with satellites. *Jupiter the Planet Satellites & Magnetosphere*, *1*, 513–536.

Kivelson, M. G., & Southwood, D. J. (2005). Dynamical consequences of two modes of centrifugal instability in Jupiter's outer magnetosphere. *Journal of Geophysical Research*, *15*, A12209. https://doi.org/10.1029/2005ja011176

Kotsiaros, S., Connerney, J. E. P., Clark, G., Allegrini, F., Gladstone, G. R., Kurth, W. S., et al. (2019). Birkeland currents in Jupiter's magnetosphere observed by the polar-orbiting Juno spacecraft. *Nature Astronomy*, *3*(10), 904–909. https://doi.org/10.1038/s41550-019-0819-7

Krupp, N., Woch, J., Lagg, A., Roelof, E. C., Williams, D. J., Livi, S., & Wilken, B. (2001). Local time asymmetry of energetic ion anisotropies in the Jovian magnetosphere. *Planetary and Space Science*, *49*(3–4), 283–289. https://doi.org/10.1016/s0032-0633(00)00149-5

Kurth, W. S. (1992). Comparative observations of plasma waves at the outer planets. *Advances in Space Research*, *12*(8), 83–90. https://doi.org/10.1016/0273-1177(92)90380-g

Kurth, W. S., Gurnett, D. A., Bolton, S. J., Roux, A., & Levin, S. M. (1997). Jovian radio emissions: An early overview of Galileo observations. In H. O. Rucker, S. J. Bauer, & A. Lecacheux (Eds.), *Planetary radio emissions IV*. Vienna: Austrian Academy of Sciences, pp. 1–13.

Kurth, W. S., Hospodarsky, G. B., Kirchner, D. L., Mokrzycki, B. T., Averkamp, T. F., Robison, W. T., et al. (2017). The Juno waves investigation. *Space Science Reviews*, *213*(1–4), 347–392. https://doi.org/10.1007/s11214-017-0396-y

Kurth, W. S., Imai, M., Hospodarsky, G. B., Gurnett, D. A., Louarn, P., Valek, P., et al. (2017). A new view of Jupiter's auroral radio spectrum. *Geophysical Research Letters*, *44*(14), 7114–7121. https://doi.org/10.1002/2017gl072889

Louarn, P., Allegrini, F., McComas, D. J., Valek, P. W., Kurth, W. S., André, N., et al. (2017). Generation of the Jovian hectometric radiation: First lessons from Juno. *Geophysical Research Letters*, *44*(10), 4439–4446. https://doi.org/10.1002/2017gl072923

Louarn, P., Allegrini, F., McComas, D. J., Valek, P. W., Kurth, W. S., André, N., et al. (2018). Observation of electron conics by Juno: Implications for Radio generation and acceleration processes. *Geophysical Research Letters*, *45*(18), 9408–9416. https://doi.org/10.1029/2018gl078973

Louis, C. K., Prangé, R., Lamy, L., Zarka, P., Imai, M., Kurth, W. S., & Connerney, J. E. P. (2019). Jovian auroral radio sources detected in situ by Juno/Waves: Comparisons with model auroral ovals and simultaneous HST FUV images. *Geophysical Research Letters*, *46*(21), 11606–11614. https://doi.org/10.1029/2019gl084799

Mauk, B. H., Clark, G., Gladstone, G. R., Kotsiaros, S., Adriani, A., Allegrini, F., et al. (2020). Energetic particles and acceleration regions over Jupiter's polar cap and main aurora: A broad overview. *Journal of Geophysical Research: Space Physics*, e2019JA027699. https://doi.org/10.1029/2019ja027699

Mauk, B. H., Haggerty, D. K., Jaskulek, S. E., Schlemm, C. E., Brown, L. E., Cooper, S. A., et al. (2017). The Jupiter energetic particle detector instrument (JEDI) Investigation for the Juno Mission. *Space Science Reviews*, *213*(1–4), 289–346. https://doi.org/10.1007/s11214-013-0025-3

McComas, D. J., Alexander, N., Allegrini, F., Bagenal, F., Beebe, C., Clark, G., et al. (2017). The Jovian Auroral distributions experiment (JADE) on the Juno mission to Jupiter. *Space Science Reviews*, *213*(1–4), 547–643. https://doi.org/10.1007/s11214-013-9990-9

Metzger, A. E., Gilman, D. A., Luthey, J. L., Hurley, K. C., Schnopper, H. W., Seward, F. D., & Sullivan, J. D. (1983). The detection of X rays from Jupiter. *Journal of Geophysical Research*, *88*(A10), 7731–7741. https://doi.org/10.1029/ja088ia10p07731

Millward, G., Miller, S., Stallard, T., Aylward, A. D., Achilleos, N. (2002). On the dynamics of the Jovian ionosphere and thermosphere III. The modelling of auroral conductivity. *Icarus*, *160*(1), 95–107. https://doi.org/10.1006/icar.2002.6951

Moriconi, M. L., Adriani, A., Dinelli, B. M., Fabiano, F., Altieri, F., Tosi, F., et al. (2017). Preliminary JIRAM results from Juno polar observations: 3. Evidence of diffuse methane presence in the Jupiter auroral regions. *Geophysical Research Letters*, *44*(10), 4641–4648. https://doi.org/10.1002/2017gl073592

21699402, 2021, 9, Downloaded from https://agupubs.onlinelibrary.wiley.com/doi/10.1029/2021JA029469 by Cochraneltalia, Wiley Online Library on [26/02/2025]. See the Terms and Conditions (https://onlinelibrary.wiley.com/terms-and-conditions) on Wiley Online Library for rules of use; OA articles are governed by the applicable Creative Commons License

Mura, A., Adriani, A., Altieri, F., Connerney, J. E. P., Bolton, S. J., Moriconi, M. L., et al. (2017). Infrared observations of Jovian aurora from Juno's first orbits: Main oval and satellite footprints. *Geophysical Research Letters*, *44*, 11–5316. https://doi.org/10.1002/2017GL072954, issue.

Nichols, J. D., & Cowley, S. W. H. (2004). Magnetosphere-ionosphere coupling currents in Jupiter's middle magnetosphere: Effect of precipitation-induced enhancement of the ionospheric Pedersen conductivity. *Annales Geophysicae*, *22*(5), 1799–1827. https://doi.org/10.5194/angeo-22-1799-2004

Perry, J. J., Kim, Y. H., Fox, J. L., & Porter, H. S. (1999). Chemistry of the Jovian auroral ionosphere. *Journal of Geophysical Research*, *104*(E7), 16541–16565. https://doi.org/10.1029/1999je900022

Sarkango, Y., Jia, X., & Toth, G. (2019). Global MHD simulations of the response of Jupiter's magnetosphere and ionosphere to changes in the solar wind and IMF. *Journal of Geophysical Research: Space Physics*, *124*(7), 5317–5341. https://doi.org/10.1029/2019ja026787

Saur, J., Janser, S., Schreiner, A., Clark, G., Mauk, B. H., Kollmann, P., et al. (2018). Wave-particle interaction of Alfvén Waves in Jupiter's magnetosphere: Auroral and magnetospheric particle acceleration. *Journal of Geophysical Research: Space Physics*, *123*(11), 9560–9573. https://doi.org/10.1029/2018ja025948

Seiff, A., Kirk, D. B., Knight, T. C. D., Young, R. E., Mihalov, J. D., Young, L. A., et al. (1998). Thermal structure of Jupiter's atmosphere near the edge of a 5-μm hot spot in the north equatorial belt. *Journal of Geophysical Research*, *103*(E10), 22857–22889. https://doi.org/10.1029/98je01766

Southwood, D. J., & Kivelson, M. G. (2001). A new perspective concerning the influence of the solar wind on the Jovian magnetosphere. *Journal of Geophysical Research*, *106*(A4), 6123–6130. https://doi.org/10.1029/2000ja000236

Stallard, T., Miller, S., Millward,G., Joseph, R. D. (2001). On the dynamics of the Jovian ionosphere and thermosphere I. The measurement of ion winds. *Icarus*, *154*(2), 475–491. https://doi.org/10.1006/icar.2001.6681

Stallard, T. S., Burrell, A. G., Melin, H., Fletcher, L. N., Miller, S., Moore, L., et al. (2018). Identification of Jupiter's magnetic equator through H_3^+ ionospheric emission. *Nature Astronomy*, *2*(10), 773–777. https://doi.org/10.1038/s41550-018-0523-z

Stallard, T. S., Miller, S., Cowley, S. W. H., & Bunce, E. J. (2003). Jupiter's polar ionospheric flows: Measured intensity and velocity variations poleward of the main auroral oval. *Geophysical Research Letters*, *30*(5), 1221. https://doi.org/10.1029/2002GL016031

Stone, R. G., Pedersen, B. M., Harvey, C. C., Canu, P., Cornilleau-Wehrlin, N., Desch, M. D., et al. (1992). Ulysses radio and plasma wave observations in the Jupiter environment. *Science*, *257*, 1524–1531. https://doi.org/10.1126/science.257.5076.1524

Sulaiman, A. H., Elliott, S. S., Kurth, W. S., Faden, J. B., Hospodarsky, G. B., & Menietti, J. D. (2021). Inferring Jovian electron densities using plasma wave spectra obtained by the Juno/Waves instrument. *Journal of Geophysical Research: Space Physics*, *126*, e2021JA029263. https://doi.org/10.1029/2021JA029263

Sundstrom, G., Mowat, J. R., Danared, H., Datz, S., Brostrom, L., Filevich, A., et al. (1994). Destruction rate of H_3^+ by low-energy electrons measured in a storage-ring experiment. *Science*, *263*(5148), 785–787. https://doi.org/10.1126/science.263.5148.785

Tao, C., Badman, S. V., & Fujimoto, M. (2011). UV and IR auroral emission model for the outer planets: Jupiter and Saturn comparison. *Icarus*, *213*(2), 581–592. https://doi.org/10.1016/j.icarus.2011.04.001

Tao, C., Fujiwara, H., & Kasaba, Y. (2009). Neutral wind control of the Jovian magnetosphere-ionosphere current system. *Journal of Geophysical Research*, *114*(A8), A08307. https://doi.org/10.1029/2008ja013966

Tao, C., Miyoshi, Y., Achilleos, N., & Kita, H. (2014). Response of the Jovian thermosphere to variations in solar EUV flux. *Journal of Geophysical Research: Space Physics*, *119*(5), 3664–3682. https://doi.org/10.1002/2013ja019411

Tetrick, S. S., Gurnett, D. A., Kurth, W. S., Imai, M., Hospodarsky, G. B., Bolton, S. J., et al. (2017). Plasma waves in Jupiter's high-latitude regions: Observations from the Juno spacecraft: Jupiter's high-latitude plasma waves. *Geophysical Research Letters*, *44*(10), 4447–4454. https://doi.org/10.1002/2017gl073073

Vasyliunas, V. M. (1983). *Plasma distribution and flow*. New York: Cambridge University Press.

Vogt, M. F., Kivelson, M. G., Khurana, K. K., Joy, S. P., & Walker, R. J. (2010). Reconnection and flows in the Jovian magnetotail as inferred from magnetometer observations: Reconnection in the Jovian magnetotail. *Journal of Geophysical Research*, *115*(A6), A06219. https://doi.org/10.1029/2009ja015098

Waite, J. H., Bagenal, F., Seward, F., Na, C., Gladstone, G. R., Cravens, T. E., et al. (1994). ROSAT observations of the Jupiter aurora. *Journal of Geophysical Research*, *99*(A8), 14799–14809. https://doi.org/10.1029/94ja01005

Wang, Y., Blanc, M., André, N., Wang, C., Allegrini, F., Blelly, P.-L., et al. (2021). A preliminary study of Magnetosphere-Ionosphere-Thermosphere coupling at Jupiter: Juno multi-instrument measurements and modelling tools. *V1. NSSDC Space Science Article Data Repository*.

Wang, Y., Guo, X., Tang, B., Li, W., Wang, C., & Wang, C. (2018). Modeling the Jovian magnetosphere under an antiparallel interplanetary magnetic field from a global MHD simulation. *Earth and Planetary Physics*, *2*(4), 303–309. https://doi.org/10.26464/epp2018028

Wibisono, A. D., Branduardi-Raymont, G., Dunn, W. R., Coates, A. J., Weigt, D. M., Jackman, C. M., et al. (2020). Temporal and spectral studies by XMM-Newton of Jupiter's X-ray auroras during a compression event. *Journal of Geophysical Research: Space Physics*, *125*, e2019JA027676. https://doi.org/10.1029/2019JA027676

Zarka, P. (1998). Auroral radio emissions at the outer planets: Observations and theories. *Journal of Geophysical Research*, *103*(E9), 20159–20194. https://doi.org/10.1029/98je01323

Zarka, P. (2004). Radio and plasma waves at the outer planets. *Advances in Space Research*, *33*(11), 2045–2060. https://doi.org/10.1016/j.asr.2003.07.055

Zhang, B., Delamere, P. A., Ma, X., Burkholder, B., Wiltberger, M., Lyon, J. G., et al. (2018). Asymmetric Kelvin-Helmholtz instability at Jupiter's magnetopause boundary: Implications for corotation-dominated systems. *Geophysical Research Letters*, *45*(1), 56–63. https://doi.org/10.1002/2017gl076315

21699402, 2021, 9, Downloaded from https://agupubs.onlinelibrary.wiley.com/doi/10.1029/2021JA029469 by CochraneItalia, Wiley Online Library on [26/02/2025]. See the Terms and Conditions (https://onlinelibrary.wiley.com/terms-and-conditions) on Wiley Online Library for rules of use; OA articles are governed by the applicable Creative Commons License